JAMES | Journal of Advances in Modeling Earth Systems

RESEARCH ARTICLE
10.1029/2024MS004791

Sensitivity of Self-Aggregation and the Key Role of the Free Convection Distance

A. Casallas[1,2,3], **A. M. Tompkins**[1], **C. Muller**[2], **and G. Thompson**[4]

[1]Earth System Physics, International Centre for Theoretical Physics, Trieste, Italy, [2]Institute of Science and Technology Austria, Klosterneuburg, Austria, [3]Department of Mathematics and Geoscience, University of Trieste, Trieste, Italy, [4]General Electrics Aerospace, Cincinnati, OH, USA

Key Points:

- The maximum free convective distance d_{clr}, is key to predict the occurrence of convective self aggregation in idealized simulations
- Horizontal and vertical diffusion impact aggregation through altering the number and size of convective cores and modifying d_{clr}
- d_{clr} is sensitive to cold pool (CP) size, as stronger CPs enhance moisture redistribution, gust front convergence, and convective onset

Supporting Information:

Supporting Information may be found in the online version of this article.

Correspondence to:

A. Casallas,
Alejandro.CasallasGarcia@ist.ac.at

Citation:

Casallas, A., Tompkins, A. M., Muller, C., & Thompson, G. (2025). Sensitivity of self-aggregation and the key role of the free convection distance. *Journal of Advances in Modeling Earth Systems*, *17*, e2024MS004791. https://doi.org/10.1029/2024MS004791

Received 24 OCT 2024
Accepted 17 FEB 2025

Author Contributions:

Conceptualization: A. M. Tompkins
Data curation: C. Muller
Formal analysis: A. M. Tompkins, C. Muller, G. Thompson
Funding acquisition: A. M. Tompkins
Investigation: A. M. Tompkins
Methodology: C. Muller, G. Thompson
Resources: A. M. Tompkins
Supervision: A. M. Tompkins, C. Muller, G. Thompson
Validation: C. Muller

Abstract Recently, Biagioli and Tompkins (2023, https://doi.org/10.1029/2022ms003231) used a simple stochastic model to derive a dimensionless parameter to predict convective self aggregation (SA) development, which was based on the derivation of the maximum free convective distance (d_{clr}) expected in the pre-aggregated, random state. Our goal is to test and further investigate this hypothesis, namely that d_{clr} can predict SA occurrence, using an ensemble of 24 distinct combinations of horizontal mixing, planetary boundary layer (PBL), and microphysical parameterizations. We conclude that the key impact of parameterization schemes on SA is through their control of the number of convective cores and their relative spacing, d_{clr}, which itself is impacted by cold-pool (CP) properties and mean updraft core size. SA is more likely when the convective core count is small, while CPs modify convective spacing via suppression in their interiors and triggering by gust-front convergence and collisions. Each parameterization scheme emphasizes a different mechanism. Subgrid-scale horizontal turbulent mixing mainly affects SA through the determination of convective core size and thus spacing. The sensitivity to the microphysics is mainly through rain evaporation and the subsequent impact on CPs, while perturbations to the ice cloud microphysics have a limited effect. Non-local PBL mixing schemes promote SA primarily by increasing convective inhibition through inversion entrainment and altering low cloud amounts, leading to fewer convective cores and larger d_{clr}.

Plain Language Summary Understanding why convective clustering and self-aggregation (SA) of clouds occurs could be crucial for our assessment of climate sensitivity. Through 24 simulations with varied settings, we explored factors contributing to SA of convection. We test the hypothesis that the chances of aggregation are related to the mean convective spacing in the initial phase of the simulation when convection is spread throughout the domain, as measured by the maximum free convective distance, d_{clr}. A large d_{clr} increases spatial humidity variability and also creates a high-pressure zone, inducing a divergent flow, and transporting moisture upgradient to moister, convective regions. d_{clr} is closely linked to the number of convection cores, influenced by factors like horizontal air mixing, moisture redistribution efficiency, low-level cloud cover, convective inhibition, rain evaporation, and cold pool intensity and size.

1. Introduction

In the early 1990s, Held et al. (1993) documented a phenomenon, now known as convective self-aggregation (SA), in 2D idealized simulations. SA denotes the tendency of convection to spontaneously organize into clusters within simulations of radiative convective equilibrium (RCE), starting from a uniformly distributed state. Subsequent research explored SA within 3D cloud-resolving models (CRMs) conducted by various authors (e.g., Beucler et al., 2020; Bretherton et al., 2005; Coppin & Bony, 2015; Grabowski & Moncrieff, 2004; Holloway & Woolnough, 2016; Huang & Wu, 2022; C. Muller & Held, 2012; Shamekh et al., 2020; Stephens et al., 2008; Tompkins & Craig, 1998; Wing & Emanuel, 2014; Wing & Cronin, 2016; Yanase et al., 2020, among others). SA typically originates with the birth of dry regions, expanding to inhibit deep convection development and confining it to specific areas in the simulation domain. This process results in reduced domain-mean water vapor and increased domain-mean outgoing longwave radiation (OLR), significantly influencing the hydrological cycle and the energy budget (e.g., Bao & Sherwood, 2019; Becker & Wing, 2020; Da Silva et al., 2021; Mauritsen & Stevens, 2015; Wing et al., 2020).

While the significance of SA is well-acknowledged, uncertainties persist in understanding its initiation and inhibition mechanisms. Past research has highlighted the role of cloud-radiative feedback (C. Muller, Yang,

Writing – original draft: A. M. Tompkins, C. Muller
Writing – review & editing: G. Thompson

et al., 2022; Stephens et al., 2008; Tompkins & Craig, 1998; Wing, 2019; Wing & Emanuel, 2014; Wing, Emanuel, et al., 2018) but several studies have also shown the uncertainty related to domain geometry (Wing & Cronin, 2016), size (Yanase et al., 2020), resolution (C. Muller & Held, 2012), surface properties (Bretherton et al., 2005), and adopted physical parameterizations (Casallas, 2024b; Shi & Fan, 2021; Silvestri et al., 2024; Tompkins & Semie, 2017; Wing & Cronin, 2016). The Radiative-Convective Equilibrium Model Intercomparison Project (RCEMIP) aimed to improve SA understanding by conducting multiple simulations with different models under standardized settings (Wing, Reed, et al., 2018; Wing et al., 2020). Convergence observed among models in several SA aspects emphasizes the importance of a comprehensive approach to understanding SA. However, the observed differences between models highlight that uncertainties may arise from, for example, variations in model physics.

To address these uncertainties, previous efforts include sensitivity (Bretherton et al., 2005; Silvestri et al., 2024; Tompkins & Semie, 2017; Wing & Cronin, 2016) and mechanisms denial experiments (Haerter et al., 2019; Jeevanjee & Romps, 2013; C. Muller & Bony, 2015; Yang, 2019). These investigations offer crucial insights into factors like radiative and evaporative cooling feedbacks (Hwong & Muller, 2024; Yanase et al., 2020), cold-pools (CPs) (Jeevanjee & Romps, 2013; Yanase et al., 2020), surface temperature gradients (Bretherton et al., 2005; Hohenegger & Stevens, 2016; Shamekh et al., 2020; Tompkins & Semie, 2021), and land surface (Hohenegger & Stevens, 2018), influencing SA emergence or hindrance. Despite their value, mechanisms denial experiments can yield intricate interpretations, as manipulating one mechanism may inadvertently affect others (Holloway, 2017).

To address the intricacies of mechanisms denial experiments, researchers have turned to simplified models (Biagioli & Tompkins, 2023; Craig & Mack, 2013; Emanuel et al., 2014; Windmiller & Craig, 2019). Notably, Biagioli and Tompkins (2023) developed a stochastic reaction-diffusion model integrated on a domain and grid resolution similar to that used in full-physics cloud resolving models. This simple model was capable of replicating both randomly distributed and aggregated states. In their work, they introduced a theory that aggregation occurred when the spatial variability in the model's thermodynamic variable was sufficient to allow the thermodynamical sensitivity of the convective triggering function to amplify this variability, despite the action of transport to remove spatial anomalies. In their model, the thermodynamic variable is column water vapor and the convective sensitivity is posed in terms of the observed precipitation-water vapor relationship in the tropics (Bretherton et al., 2004; Rushley et al., 2018) but the sensitivity acts as a proxy for all feedbacks, including cloud-radiative diabatic forcing. Based on this premise, Biagioli and Tompkins (2023) develop a dimensionless index, named the aggregation number (N_{ag}), that predicts if the model will undergo SA, based on the model domain size, resolution, moisture transport/diffusion, convective core density, and the subsidence timescales. Key to N_{ag} is the combination of several of these ingredients to predict the largest clear sky area (d_{clr}) in the pre-onset state. Their findings predict that a reduced number of convective cores, associated with larger inter-convective spacing (d_{clr}), promotes the development of SA. The increased separation of convective moisture sources leads to greater spatial moisture variability which can then be amplified by the moisture-sensitive convective parameterization if it exceeds a critical threshold.

The model of Biagioli and Tompkins (2023), despite reproducing several characteristics of the full physics models, such as bi-stable random and clustered equilibria, and similar sensitivities to domain size and resolution, remains a highly idealized model. The question therefore arises as to whether elements of N_{ag} can also be applied to successfully predict SA in the full-physics models. In this paper, we focus on the role of d_{clr} and its implications for SA in full physics models, in particular the anti-correlation between d_{clr} and the number of convective cores.

Our approach is to examine the sensitivity of the Weather Research and Forecasting (WRF) model SA to perturbations in various parameterizations of physical processes, to see if these can be interpreted in terms of their relative impact on d_{clr}. Horizontal and vertical mixing (Cohen & Craig, 2004, 2006; Tompkins & Semie, 2017) have been show to play a role in modifying low-clouds, convective inhibition, convective core number, d_{clr}, and consequently impacting SA dynamics. CPs influence SA through their horizontal redistribution of moisture in the boundary layer and convective triggering at their edge. CPs also induce localized drying near their center, affecting the distance between cores and d_{clr}. Thus, changes to physical processes such as rainfall evaporation could also be expected to impact SA through CP impacts. Our study focus on the specific impact of different parameterizations within a CRM, including microphysics, sub-grid scale mixing, and planetary boundary layer (PBL) schemes, on d_{clr} and, by extension, SA. The overarching goal is to uncover the sensitivities and interactions

governing SA's behavior, revealing its intricate interplay with atmospheric variables. Given this context, this study posits the following question:

- What is the sensitivity of SA development to the processes that control convective triggering and thus d_{clr} and can this be used to explain how those parameterizations of the model physics impact SA?

The next section describes the CRM setup used in the simulations, a brief explanation of the parameterizations utilized in the experiments, as well as the diagnostics. Section 3 contains the results, starting from an overview (Section 3.1), then we focus on studying the dry patches evolution (Section 3.2), which leads to the importance of d_{clr}. Subsequently, we make a thorough explanation of the mechanisms (Section 4) that control the number of convective cores and d_{clr} for the sub-grid scale mixing (Section 4.1), the microphysics (Section 4.2), and the PBL (Section 4.3) schemes. Concluding remarks are presented in Section 5.

2. Method

2.1. Model Description

We utilize version 4.2 of the WRF model (Skamarock et al., 2019) for all simulations. The model employs a fifth-order horizontal advection scheme and we apply Rayleigh damping at 10 km to prevent unphysical wave reflection (Skamarock et al., 2019). The RRTMG scheme (Iacono et al., 2008; Mlawer et al., 1997) is used to represent longwave (LW) and shortwave (SW) radiative transfer. The surface layer scheme follows Monin-Obukhov similarity theory (Monin & Obukhov, 1954), considering stability functions and roughness lengths. We select three sub-grid scale schemes, two PBL schemes, and four microphysics schemes, that are briefly described below.

2.2. Sub-Grid Scale Mixing Schemes

We choose three commonly employed sub-grid scale schemes: Smagorinsky-2D (Smag2), Smagorinsky-3D (Smag3) (Smagorinsky, 1963), and the turbulent kinetic energy (TKE) scheme. Smag2 operates solely in the horizontal plane, relying on turbulent kinetic energy generated from horizontal shear, so the vertical mixing is represented by the PBL scheme. Conversely, Smag3, calculates mixing using both the full 3D wind shear and static stability, enabling it to function independently and in combination of a PBL scheme. The TKE scheme (Skamarock et al., 2019) employs a 1.5 closure that accounts for both horizontal and vertical mixing, with the prognostic equation encompassing shear production, buoyancy, transport, and dissipation terms. These three schemes are selected due to their documented varied aggregation behaviors in prior studies, attributed to differences in entrainment magnitudes (Tompkins & Semie, 2017).

2.3. Planetary Boundary Layer

We select two PBL schemes: the Yonsei University scheme (YSU) and the Bougeault-Lacarrere Scheme (BouLac). YSU, a non-local PBL scheme (Hong & Pan, 1996; Hong et al., 2006), has undergone extensive numerical evaluations (Hu et al., 2010; Noh et al., 2003). Its non-local mixing capability allows it to represent vertical mixing throughout the troposphere (Potvin et al., 2020). On the other hand, BouLac, a 1.5-order local scheme (Bougeault & Lacarrere, 1989; Therry & Lacarrère, 1983), is chosen because local schemes often exhibit insufficient moisture mixing within convective cores. For a more comprehensive understanding of the PBL schemes, readers are directed to Supporting Information S1 (Text S2).

2.4. Microphysics Schemes

We conducted simulations employing four microphysical schemes: WRF Single Moment 6-Class (WSM), Goddard Cumulus Ensemble (GCE), Thompson (Tho), and Morrison (Mor) schemes. WSM, a single-moment scheme (Dudhia, 1989; Rutledge & Hobbs, 1983), incorporates modifications to the graupel class and ice representation (Dudhia et al., 2008; Hong & Lim, 2006; Hong et al., 2004). GCE (Tao & Simpson, 1993), another single-moment scheme, is based on Lin et al. (1983) with numerous modifications outlined in Tao et al. (2014) and Lang et al. (2014). Tho is a hybrid scheme, utilizing single-moment for cloud water which follows the observations of Martin et al. (1994), it also uses single-moment on snow (Field et al., 2007) and graupel and double-moment for rain and cloud ice (Iverson et al., 2021; Thompson et al., 2008). Mor (Morrison & Gettelman, 2008; Morrison & Pinto, 2006; Morrison et al., 2005) is a full double-moment bulk microphysics scheme predicting

number and mass mixing ratios for six hydro-meteor species, allowing a more robust and realistic treatment of particle size distributions. Table S1 in Supporting Information S1 outlines the principal characteristics of the microphysics schemes, including fall speed constants and size and number distributions with their corresponding intercept parameters. For a detailed explanation of each microphysical scheme, readers are directed to Text S2 in Supporting Information S1.

2.5. Simulation Setup

The model domain is $O(510\ \text{km})^2$ in the horizontal with periodic boundary conditions, a fixed sea surface temperature of 301 K as in Tompkins and Semie (2017) and with a 3 s time step. The domain size is selected since smaller domains could disallow SA from happening (Biagioli & Tompkins, 2023; C. Muller & Held, 2012; Yanase et al., 2020). It also uses a $(2\ \text{km})^2$ horizontal resolution to explicitly resolve convection (Bretherton et al., 2005; Tompkins & Craig, 1998; Tompkins & Semie, 2021), and has a stretched vertical grid (62 levels) (Tompkins & Semie, 2017). The diurnal cycle is active, there are no Coriolis effects, and no mean wind was imposed.

We perform several experiments to study the impact of the sub-grid scale mixing, PBL, and microphysics schemes on convective SA. The experiments last for 45 days with hourly outputs. They consist of the combination of three sub-grid scale schemes, with two PBL schemes and four microphysics schemes, which means that 24 simulations were performed. The nomenclature of the simulations is as follows: First the microphysics scheme used (e.g., Tho, GCE), second the sub-grid scale mixing scheme (i.e., "TKE" for TKE, "SM3" for Smag3 and "SM2" for Smag2), and third the PBL ends the nomenclature, either YSU or BL for the BouLac scheme. For instance, if the simulation uses Thompson microphysics with Smag2 and YSU, the simulation name would be Tho-SM2-YSU, but if the horizontal mixing is Smag3 with BouLac the name would be Tho-SM3-BL.

The initial conditions in our study were adopted from Jordan (1958). In addition to our 24 primary experiments (Table S2 in Supporting Information S1), we conducted five (5) sensitivity simulations, depicted in Table S3 in Supporting Information S1, for a total of 29 experiments. The first, denoted Tho-SM2-BHE, involved a 50% reduction in rain evaporation within the Tho-SM2-BL configuration. In the second, Tho-SM2-YDE, we doubled the rain evaporation within the Tho-SM2-YSU setup. The third, Tho-SM2-YHI, entailed a 50% reduction in the fall speed of ice/snow within the Tho-SM2-YSU configuration. The fourth, Tho-SM2-BDI, involved doubling the fall speed of ice/snow within the Tho-SM2-BL configuration. Finally, the fifth, Tho-SM-YNL, remove the low-level clouds from the longwave radiation calculation by zeroing the liquid condensates.

2.6. Maximum Free Convection Area d_{clr}

To assess the spatial extent of free convective regions, we calculated a metric that quantifies the maximum distance between convective sources, d_{clr}, highlighting the largest convectively inactive area within the model domain. Convective sources were identified as grid points where the vertical velocity (w) exceeded 1 m s^{-1} at 750 hPa (Tompkins & Semie, 2017). For each time step, the coordinates of these convective sources were extracted, and periodic boundary conditions were accounted for by replicating the domain eight times in neighboring directions. This ensured continuity across boundaries and avoided edge effects (Biagioli & Tompkins, 2023).

Distances were computed between all convective grid points and their nearest neighboring convective source using an efficient spatial querying method (Maneewongvatana & Mount, 1999, cKDTree algorithm). The maximum of these distances defines the largest free convective region, d_{clr}, consistent with the concept of $d_{\text{max},clr}$ depicted in Figure 8 of Biagioli and Tompkins (2023).

2.7. Tracking Algorithm

To investigate the role of CPs in the development of SA, we track and analyze their characteristics using a Lagrangian tracker, which is also employed to monitor the evolution of dry patches. The tracker is based on the standard watershed algorithm, as described by Casallas et al. (2024), and utilizes the Scikit-image library version 0.16 (Virtanen et al., 2020) in Python 3.6. Initially, the algorithm segments the image such that each segment corresponds to a unique object, based on a specific threshold. For tracking CPs, we calculate the 2 m temperature gradient, using the 60th percentile of this gradient as a threshold on an hourly basis. To determine this threshold,

we apply a randomized search method, performing multiple tests to identify the optimal value. This approach follows a similar strategy to the one used by Drager and van den Heever (2017) in selecting the CP threshold for their algorithm. Our objective was to choose a threshold that would accurately capture the largest number of CPs while avoiding the misidentification of random regions with strong temperature gradients, as well as preventing false identifications caused by changes in gradients due to the diurnal cycle embedded in our simulations.

For the dry-patch tracking, we use the total column water vapor ($TCWV$) field and apply a threshold of 44 kg m^{-2} every hour. This threshold is also determined through a randomized search, which involves multiple tests aimed at identifying dry regions that grow gradually over time, rather than centers of CPs that might be excessively dry or isolated random dry patches that appear intermittently. This approach mirrors moisture tracking algorithms, where thresholds are selected to monitor atmospheric moisture (Stohl et al., 2005). Examples of our tracking method can be seen in Figure S1 in Supporting Information S1.

In terms of temporal tracking, the algorithm is adapted from previous Lagrangian trackers (see S. Muller, Caillaud, et al., 2022, for tracking examples) designed to track the motion of storms. The approach involves following the motion of each labeled object using velocities to predict the feature location in subsequent time-steps. These predictions are then compared to the location of actual object at this future time-slice, and if the objects Euclidean distance (of their centers and boundaries) is less than 4 km (2 pixels) and if the objects overlap, the tracker decides whether to maintain the object or assign a new label. Similar results are produced using a Euclidean distance of 2 or 6 km.

To study the pre-onset conditions, we implement a back-propagation technique: Once a dry patch reaches an area of (16 km)^2, we select its center and create a buffer with a radius of (20 km), centered around the core of the dry patch (varying buffer sizes yield similar results). We then save the coordinates of the pixels within this buffer for subsequent analysis of the atmospheric properties in the locations where dry patches form before their initial appearance.

2.8. Cold Pool Properties

CP intensity is calculated (e.g., Grant & van den Heever, 2018) by integrating the negative buoyancy as $C^2 = 2\int_0^H \left(-g\theta_v'/\overline{\theta_v}\right) dz$ (Benjamin, 1968), where C is the CP intensity, H is the height of the CP, g is the gravitational acceleration, θ_v' is the virtual temperature perturbation and $\overline{\theta_v}$ is the virtual temperature averaged over the model domain. The CP top is defined as the highest altitude where the buoyancy threshold of -0.005 m s^{-2} remains valid (Grant & van den Heever, 2016), constrained to a maximum of 2 km (16th model level) (e.g., Abramian et al., 2022).

2.9. Dry to Moist Regions Circulation

Previous studies have highlighted the significance of low clouds in dry regions for the development of SA (C. Muller & Bony, 2015). Since Section 4.3 will elucidate the importance of low-level clouds, we further analyze their role by computing the approximate stream function Ψ as introduced by Bretherton et al. (2005). Ψ serves as a useful metric for quantifying the circulation between dry and moist regions. It is computed by ordering the columns based on TCWV-percentile and calculating the corresponding mass flux for each column, as outlined in Equation 1:

$$\Psi(i,z) = \Psi(i-1,z) + \sum_{TCWV \in (TCWV_{i-1}, TCWV_i)} w(z)\overline{\rho}(z) \tag{1}$$

with $\Psi(0,z) = 0$ for every z, where $\overline{\rho}$ is the reference density profile used in the anelastic governing equations, w represents the vertical velocity, and i denotes the $TCWV$ column index. $\Psi(i,z)$, as explained by C. Muller and Held (2012), represents the total vertical mass flux across all columns where $TCWV \leq TCWV_i$. This circulation must be interpreted independently of physical space due to the $TCWV$ ordering but provides valuable insights into the exchange between dry and moist regions (Shamekh et al., 2020; Yanase et al., 2020).

3. Self Aggregation

3.1. Self-Aggregation in the Simulation Ensemble

As expected from prior research, SA exhibits a pronounced sensitivity to the parameterizations used (Figure 1). This is evident in the *TCWV* distribution across the 24 principal experiments, shown for days 10 and 40 of the simulations. The maps highlight significant variability in *TCWV* evolution across different model configurations, both in the occurrence of SA and the rate at which it develops. In general, those configurations which lead to aggregation do so by the up-scale growth of dry patches, leading the convection to be constrained to fewer regions as the simulations progress.

In some experiments the evolution appears to be extremely fast, with evidence of high spatial *TCWV* variability already by day 10, and the convection restricted to a single area by day 40, such as the experiments using Smag3. In other experiments, the onset is much slower, with the first signs of SA appearing around day 15 via numerous dry areas which are still in the process of growth at day 40. We note that all the experiments which show no sign of aggregation undergo a general drying as the simulation progresses, and appear to have a lower maximum *TCWV* even in the convecting localities. As expected from previous work of Tompkins and Semie (2017), simulations employing the Smag3 scheme exhibit rapid aggregation, in contrast to Smag2 and TKE, where SA emerges primarily when YSU is employed as the PBL scheme. This suggests a significant role of the sub-grid scale mixing and the PBL in triggering SA.

Figure 2 provides a summary, presenting the SA index calculated as the mean over the last 5 days of each experiment of the difference of the ninetieth (90th) minus tenth (10th) percentiles (hereafter NMTP) of *TCWV* (Bretherton et al., 2005; Müller & Hohenegger, 2020). The significant impact of horizontal mixing is clear, since regardless of variations in the PBL and microphysics configurations, all the Smag3 simulations develop aggregation. In comparison, the choice of microphysics scheme has a more nuanced impact on SA. Simulations using the Mor scheme appear to be slightly more likely to exhibit SA (with Mor-TKE-BL just starting to shown sign of aggregation by day 40 in Figure 1), while four of the six simulations employing the WSM scheme remain in a uniformly random configuration. The approach used for the vertical mixing can also influence SA. Simulations employing non-local PBL schemes (YSU) tend to promote SA, whereas those utilizing local schemes (BouLac) tend to inhibit SA—except in cases where microphysics dominate the driving of SA. The details of how these schemes affect SA will be examined in Section 4.

It is important to note that our simulations were conducted over 45 days. Previous studies have shown that SA can develop over longer time periods, such as 60 days or more (Holloway & Woolnough, 2016; Tompkins & Semie, 2021). To address this, we extended to 60 days three simulations that did not exhibit SA during the initial 45 days (Tho-SM2-BL, WSM-SM2-YSU, and WSM-SM2-BL), yet no signs of SA emerged during the extended period. While these results suggest robustness in our findings, it remains possible that SA could develop beyond 45 days in some simulations or beyond 60 days in others. Nonetheless, the conclusions of this paper remain valid, as they focus on the mechanisms that either favor, suppress or significantly delay the development of SA.

3.2. Dry Patches Analysis

We hypothesize that the sensitivity of SA to various parameterizations can be clarified by considering d_{clr} (Biagioli & Tompkins, 2023). The properties of convective updraft cores are intricately governed by multiple physical processes embedded within sub-grid parameterizations. To test this, we examine the TCWV-NMTP (mean of the last 5 simulations days) as a function of the mean d_{clr} calculated between days 2 and 5 (the first 48hr are discarded for model spin-up), a period that precedes the onset of SA and during which deep convection is found throughout the simulation domain. The mean CP intensity between days 2 and 5 (Figure 3) is also examined. We tested the sensitivity of the diagnostics by calculating them over different time frames (e.g., 2–3, 2–4, and 2–7 days) but no significant sensitivity to these changes was observed.

Figure 3 reveals that simulations developing SA (blue-green colors) consistently exhibit higher values of d_{clr} in the pre-onset phase, irrespective of the specific parameterizations employed. This observation agrees with the theoretical framework of Biagioli and Tompkins (2023), which posited that greater spacing between cores generates drier regions between convective moisture sources, setting the stage for the emergence of SA, and also with Silvestri et al. (2024) in two distinct CRMs. Simulations employing the Smag3 horizontal mixing scheme exhibit the largest d_{clr}. A comparison between GCE-SM2-YSU, Tho-SM2-YSU, and Tho-TKE-BL simulations,

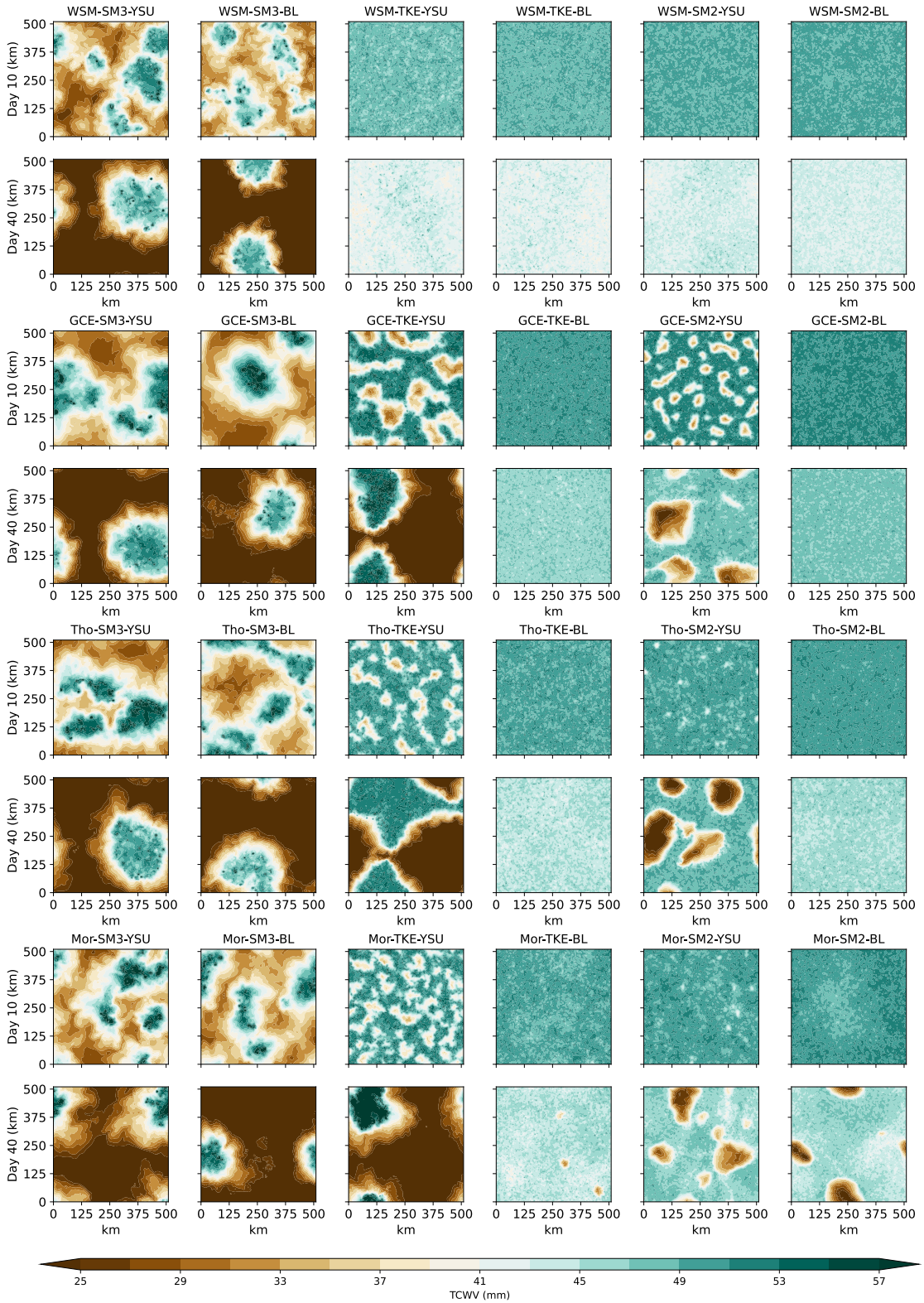

Figure 1. Snapshot of *TCWV* of all the 24 principal experiments performed (see Table S2 in Supporting Information S1). The columns represent the different model configurations. Each microphysics scheme is represented by two rows with the first depicting a snapshot of day 10, and the second showing a snapshot of day 40.

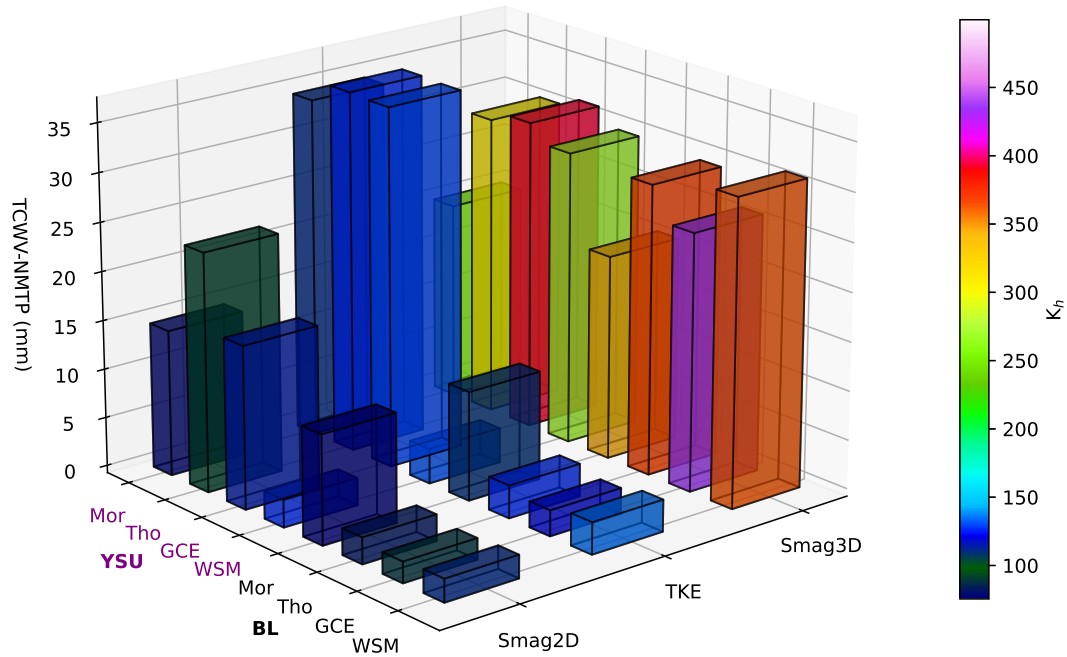

Figure 2. The height of the bars represents the mean TCWV-NMTP (calculated as percentile 90—percentile 10 of $TCWV$ and used as SA metric) between days 40 and 45 of each simulation. The colors show the mean horizontal eddy viscosity K_h inside the convective cores during the entire simulation. The x-axis shows the Sub-Grid Scale mixing scheme. The y-axis includes the microphysical parameterization and the PBL schemes. The purple font represents the simulations that use YSU and the black font the experiments using BouLac.

with comparable d_{clr} values, highlights the contrasting effect of CP intensity on SA. While Tho-TKE-BL's more intense CPs hinder SA, this is not the case for the other two simulations.

We use the Lagrangian tracker to examine the pre-onset conditions and the subsequent growth and maintenance of dry patches (Figure 4) in the Smag2 simulations (results are consistent with those simulations using TKE and Smag3 that also undergo SA). At the initial stages of the simulation, a marginally positive pressure anomaly triggers dry patch development (Figure 4d, Figures S2–S4 in Supporting Information S1). This anomaly is prominently observed in regions characterized by large d_{clr} values, which are typically drier areas. This positive pressure anomaly gradually strengthens (Yang, 2018; Yao et al., 2022) and induces a divergent flow, as detailed by Shamekh et al. (2020), facilitating the transport of moist static energy (MSE) away from the dry and into the moist regions, thus upgradient. This implies that dry regions tend to become drier, while moist regions become moister, thereby reinforcing the high-pressure anomaly and its associated divergent flow. This feedback mechanism, in turn, contributes to the expansion of the dry zone. As illustrated in Figure 4d, the initial signs of slightly positive anomalies emerge around day 2, after which the anomaly intensifies and extends throughout the entire boundary layer.

Assuming hydro-static balance, the surface pressure anomaly is related to the column density anomaly, itself related to the virtual temperature anomaly (Shamekh et al., 2020). Neglecting second order terms, Shamekh et al. (2020) decompose the virtual potential temperature $\left(\theta_v^{'}/\overline{\theta_v}\right)$ anomaly into two distinctive components within the boundary layer: the moist component $\left[0.61q_v^{'}/\left(1 + 0.61\overline{q_v}\right)\right]$ and the temperature component $\left(T^{'}/\overline{T}\right)$. The pressure anomaly is intricately linked to density anomalies within the boundary layer in tropical regions where the Coriolis parameter is relatively small, and mid and upper tropospheric density anomalies remain negligible (Sobel et al., 2001).

During the initial 20 days of the simulation, the average dry patch surface moisture anomaly (Figure 4b) becomes more pronounced over time, while the surface temperature anomaly (Figure 4c) shows a positive trend. These tendencies are compensatory in terms of buoyancy; initially, the temperature contribution dominates in the boundary layer up to around 500 m, resulting in a positive $\theta_v^{'}/\overline{\theta_v}$ anomaly (Figure 4a). However, as surface dryness intensifies probably due to enhanced radiative cooling, larger subsidence occurs in the region. This

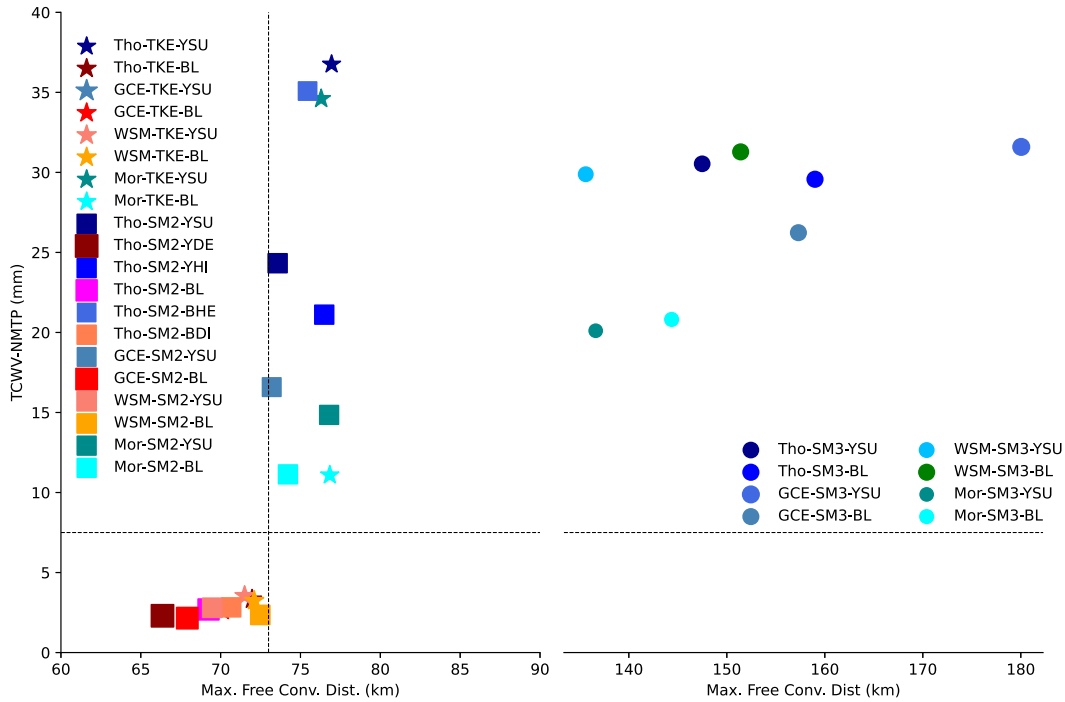

Figure 3. Mean TCWV-NMTP (calculated as in Figure 2) between day 40 and day 45 for each simulation as a function of the d_{clr}, which is averaged from day 2 to day 5 for all the experiments. The circles represent the Smag3 experiments, stars account for the TKE runs and the squares show the Smag2 simulations. The blue-green colors represent the experiments that develop SA, and red-yellow colors account for runs with random convection. The size of the markers depends on the CPs intensity averaged from day 2 to day 5, so larger markers imply stronger CPs. For conciseness, the x-axis is divided into two separate length-scale zones.

happens since, as reported by Mapes (2001), in the tropics, neglecting temperature changes and horizontal advection simplifies the thermodynamic equation to $w\alpha \approx h_r$, where w represents the vertical velocity, α denotes the static stability parameter, and h_r signifies the heating rate. Additionally, the ratio $T'/\overline{T}$ increases at a slower rate compared to atmospheric dryness. Consequently, a negative $\theta_v'/\overline{\theta_v}$ anomaly begins to form around day 7 and persists thereafter (Hwong & Muller, 2024).

This phenomenon could be attributed to the divergent flow and the associated export of MSE from dry to moist regions, particularly within the boundary layer, consistent with Shamekh et al. (2020). This is illustrated in Figure 5, that shows the stream function, Ψ, which highlights the circulation patterns, with positive values indicating clockwise flow and negative values denoting counterclockwise flow. The alignment of this circulation with the $TCWV$ gradient reflects the role of divergent flow in sustaining the dry patches.

The transition to a surface negative $\theta_v'/\overline{\theta_v}$ anomaly favors SA and leads to an accelerated rise in the pressure anomaly through the column, since moisture anomalies are strongly related with pressure changes, consistent with the weak temperature gradient approximation (Sobel et al., 2001), as evident from day ≈7 in Figure 4d. Notably, these findings align with the results obtained from experiments utilizing alternative microphysics schemes, as depicted in Figures S2–S4 in Supporting Information S1, and with the existing literature (e.g., Naumann et al., 2019; Yang, 2019).

According to Shamekh et al. (2020), the growth of a dry anomaly and the subsequent development of a high-pressure anomaly in dry areas of the PBL are primarily driven by enhanced radiative cooling (Q_{rad}), which through strong compensating subsidence, would strongly dry the local environment. Figure 6 (see Figures S5–S7 in Supporting Information S1 for other microphysics results) illustrates the temporal progression of Q_{rad}, including all its components. The net Q_{rad} (Figure 6g) anomaly exhibits strong negative values at the surface, within the altitude range of 2–5 km, and from 6 to 10 km. These regions align well with the heights of high-pressure anomalies depicted in Figure 4d.

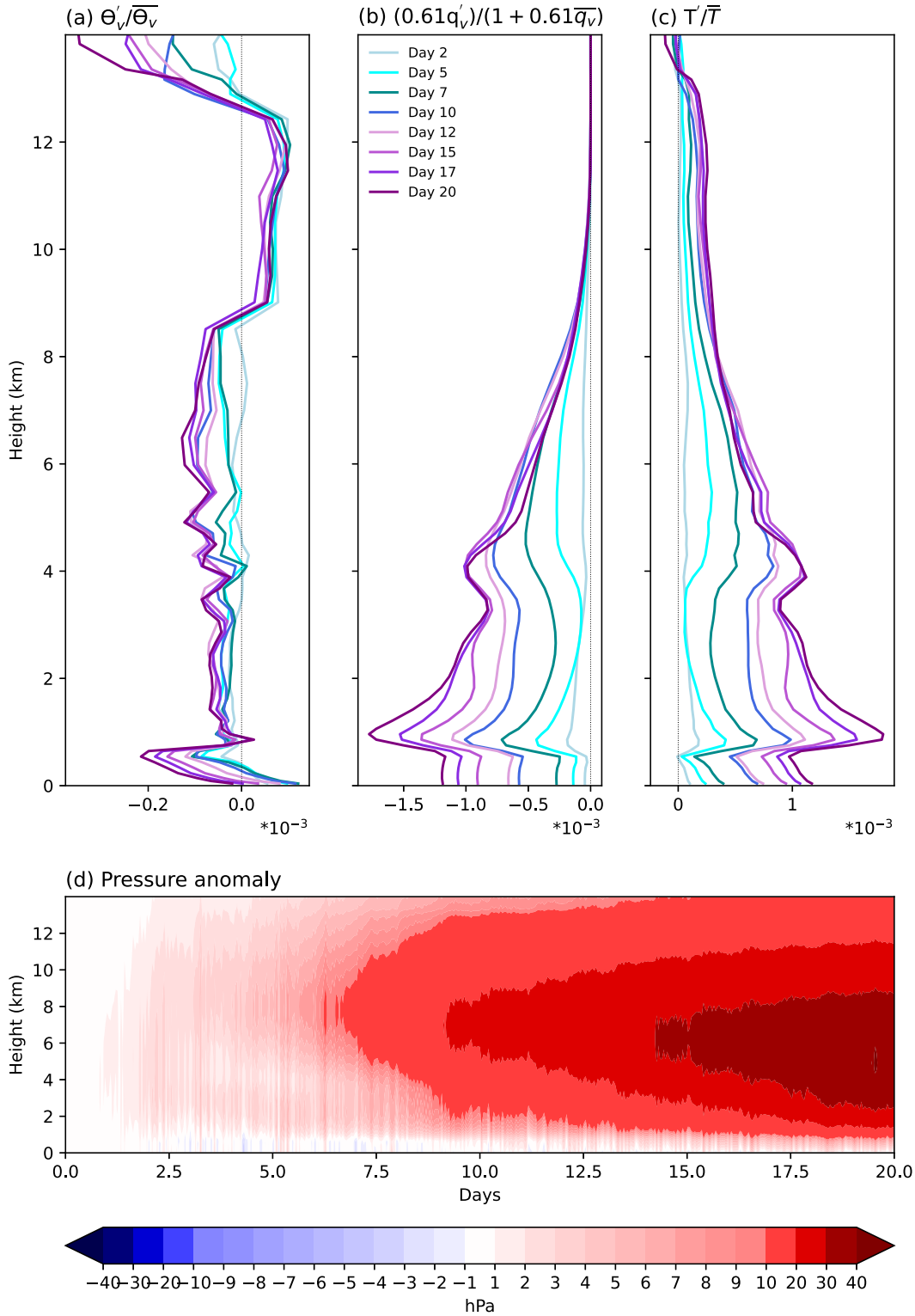

Figure 4. The plot shows daily dry patch composite means of the virtual potential temperature anomalies (a), the contributions to this variable from the q_v anomaly (b) and the temperature anomaly (c) of the Tho-SM2-YSU experiment. The results are similar for the other runs that develop SA. (d) Hourly composite of pressure anomaly from the dry patches as they evolve with time.

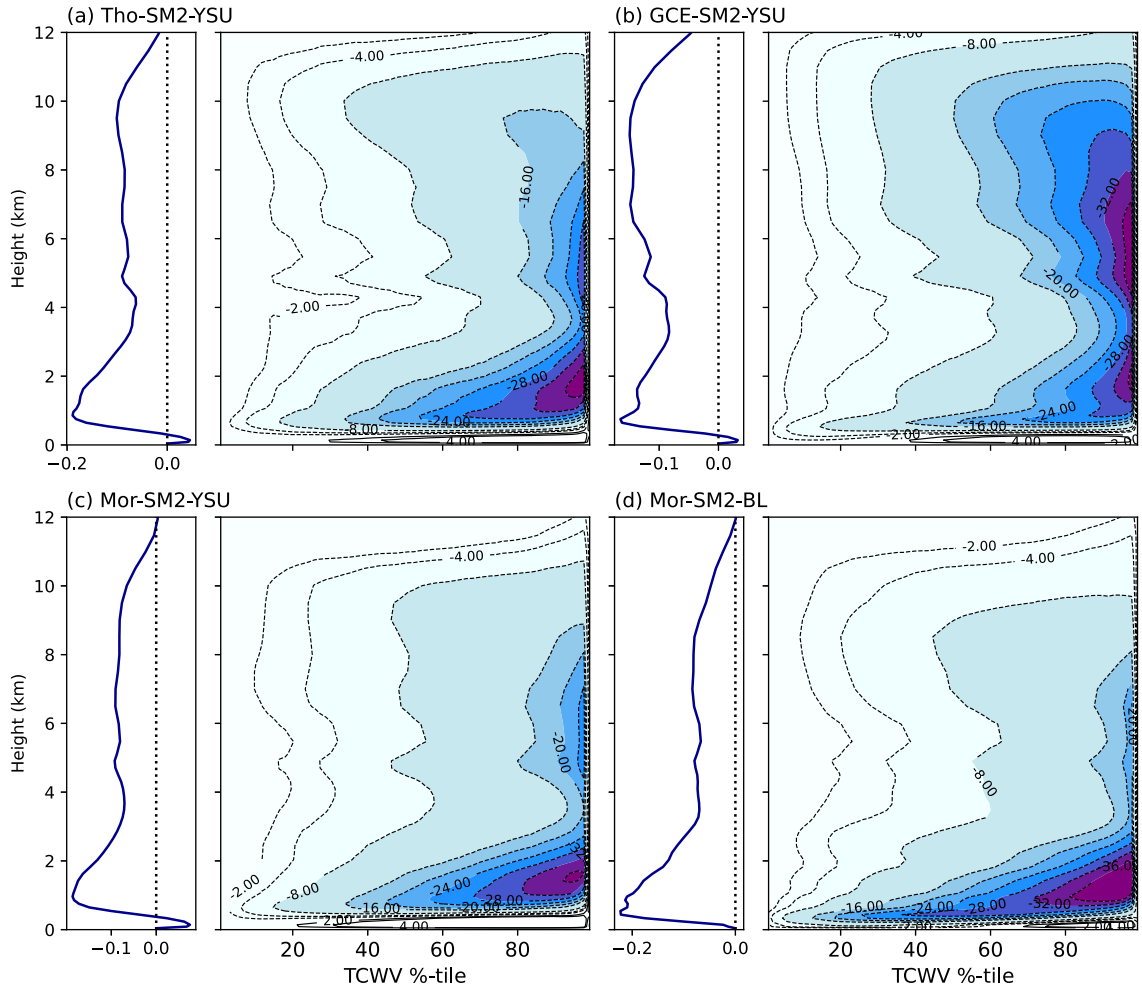

Figure 5. Stream function, Ψ, for the dry patches (colors and dashed contours) for (a) Tho-SM2-YSU, (b) GCE-SM2-YSU, (c) Mor-SM2-YSU, and (d) Mor-SM2-BL between day 2 and day 5 of the simulations. The dark blue lines at the left of the contour plots depict Ψ averaged over the domain (units 10^{-2} kg m^{-2} s^{-1}).

The cooling at the surface seems to be a consequence of the combined effects of both LW cloud radiative effect—CRE—(Figure 6a) and LW clear-sky radiative cooling (Figure 6b). This combined cooling is probably inducing a surface divergent flow, directing air from the dry patches toward the moister zones. These findings align with previous research (e.g., C. Muller & Bony, 2015; C. Muller, Yang, et al., 2022; Shamekh et al., 2020), which highlights the importance of radiative cooling from clouds. However, this is not always the case. For example, Holloway and Woolnough (2016) showed that low-level convergence is not driven by radiative cooling, suggesting that the underlying mechanisms are not fully understood, but the Lagrangian framework used in this study to track dry regions could provide valuable insights. On the other hand, the net Q_{rad} between altitudes of 2 and 5 km is primarily driven by the LW clear-sky component, regardless of the warming produced by the SW CRE component (Figure 6e). The enhanced radiative cooling produce drying and cooling in the boundary layer through subsidence (Mapes, 2001), contributing to the formation of a high-pressure anomaly at this height (Figure 4d), which initiates around day 3.

As for the net Q_{rad} anomaly between altitudes of 6–11 km, it is mainly driven by the LW CRE component, although the SW clear-sky component plays a smaller role (Figures 6b–6f). The LW CRE invokes a cooling anomaly at this height, increasing with altitude due to cloud-related processes, with its most significant values observed between 8 and 10 km, coinciding with the location of the high-pressure anomaly (Figure 4d) responsible for initiating a divergent flow at the same altitude around day 5. This divergent flow leads to the export of MSE from dry to moist regions. These two divergent branches (surface; 6–10 km), and the convergent one (2–5 km) described here and in Figure 5 resemble the circulations reported by C. Muller and Held (2012), Shamekh

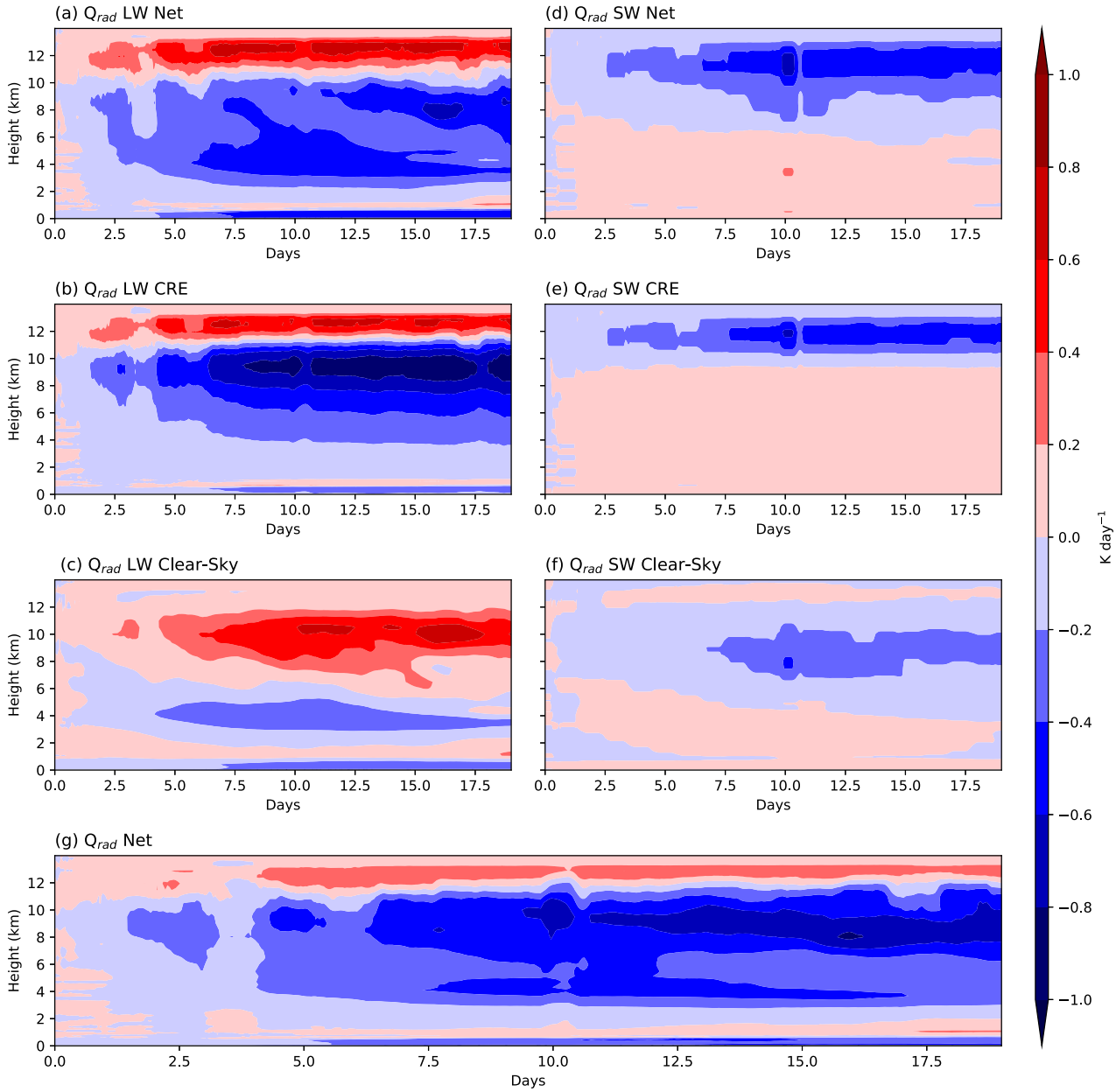

Figure 6. The plot shows dry patch composite mean evolution of the Q_{rad}. (a) LW Net (b) LW CRE, (c) LW Clear-Sky, (d) SW Net, (e) SW CRE, (f) SW Clear-Sky, and (f) the full Q_{rad} cooling perturbation for Tho-SM2-YSU. All fields are subject to a 24 hr-running mean.

et al. (2020), and Cerlini et al. (2023) when convection is clustered due to the upgradient MSE transport. It is important to notice that the results describe here also hold for the other experiments, as shown in Figures S5–S7 in Supporting Information S1.

To summarize, in simulations with large d_{clr}, the large dry regions between convective cores have prevailing subsidence, which helps trigger the well-known SA feedbacks. Large d_{clr} provides the seed for the emergence and strengthening of a dry area. Once this is done, SA feedbacks initiate and strengthen the dry area, possibly through a radiatively induced subsidence drying. We further decompose this process by examining individual physical contributions, such as virtual potential temperature, humidity, temperature anomalies, and associated pressure anomalies. Specifically, in dry patches, we observe a negative LW Q_{rad} anomaly (stronger cooling) at three distinct altitudes, as well as a negative SW clear-sky Q_{rad} anomaly in the mid-troposphere. The cooling effects from these anomalies seem to be linked to the pressure anomaly, which is intricately tied to density changes in the

boundary layer. These components together establish a divergent flow that is linked with the circulation represented by the stream function (Figure 5), driving moisture export from the dry region and reinforcing the already dry conditions. This process, ultimately, leads to the self-aggregation of the dry patch, further amplifying the feedback loop.

4. Sensitivity to Model Parameterizations

In this section we examine the results of the physics scheme perturbations in terms of their impact on d_{clr}.

4.1. Sensitivity to Sub-Grid Scale Mixing

One of the strongest sensitivities noted in the physics perturbation ensemble was the response to the subgrid-scale horizontal mixing scheme, with simulations using the 3D Smagorinsky scheme (Smag3, Figure 2) consistently developing SA, regardless of the chosen PBL or microphysics schemes. Figure 2 showed the mixing coefficient K_h, and confirmed the findings of Tompkins and Semie (2017) with K_h one order of magnitude larger in convective cores (where vertical velocity $w \geq 1$ m s^{-1} at 750 hPa) in Smag3 simulations compared to TKE or Smag2 schemes. Tompkins and Semie (2017) and Silvestri et al. (2024), point out that high K_h within convection implies greater entrainment, increasing updraft sensitivity to water vapor anomalies, and thus encouraging SA (see also Bretherton et al., 2005; Cerlini et al., 2023; Stephens et al., 2008; Tompkins & Semie, 2017; Yang, 2019).

In addition to the direct impacts of entrainment sensitivity, there is a second potential explanation: altering the mixing strength, and consequently entrainment mixing, also influences the mean size and mass flux of convective updrafts. This change, in turn, affects the number of convective cores and, consequently, d_{clr} during days 2–5 in the pre-onset phase of SA of the simulations (Figure 7).

The Smag3 simulations exhibit pronounced entrainment through enhanced K_h within convective cores (Figure 7a), resulting in a notable reduction in core count (Figure 7c), consistent with Silvestri et al. (2024). The larger core areas ($\approx 17 \pm 1.5$) km^2 in Smag3, 3–4 times larger than on the other simulations others ($\approx 3.5 \pm 1$) km^2, can be linked to the requirement for convective mass flux equilibrium in RCE scenarios (Cohen & Craig, 2004, 2006). This leads to a reduced core count necessary to offset Q_{rad}, thereby contributing to a decrease in core number, since the vertically integrated Q_{rad} remains consistent across all experiments before SA attains full development (not shown). The observed increment in mean convective core area translates to a diminished core count and, concomitantly, an increase in d_{clr} due to their inverse relationship (Figures 7b and 7c).

Thus, the association between strong entrainment, reducing core counts, and increasing d_{clr}, offers a explanation for the horizontal mixing simulations results that differs from Tompkins and Semie (2017). Our reinterpretation is that the key impact of enhanced entrainment mixing on SA is not through the sensitivity of updraft buoyancy to water vapor perturbations, but instead through the fact that it leads to wider, fewer updrafts that, on average, are more distant from each other as a result. The key impact then is a reduction in the efficiency of convective updrafts to moisten the domain (fewer local moisture sources). One of the weaknesses of the original water vapor entrainment sensitivity argument of Tompkins and Semie (2017) is that the dry patches were shown to develop from the upper troposphere first, and then deepen toward the surface. As humidity is very low in the upper troposphere, the impact of weak initial spatial variations of water vapor on updraft buoyancy would likely be minimal. This reinterpretation of the sensitivity of SA to sub-grid horizontal mixing does not rely on updraft entrainment sensitivity.

4.2. Sensitivity to the Microphysics

Since both Smag2 and TKE schemes exhibit SA under identical PBL and microphysics configurations (Figure 2), for simplicity here we focus on the simulations that use Smag2 to assess the sensitivity to microphysics (similar results are obtained with the simulations that use the TKE scheme, as shown by Figure S8 in Supporting Information S1).

Microphysics could be envisaged to impact SA through a wide variety of mechanisms. Previous work has shown that anvil cloud longwave forcing provides an atmospheric heating anomaly, which drives convergence into the convective areas (Wing & Emanuel, 2014). This is usually the strongest forcing for SA in the early period of simulations when spatial humidity variability is too weak to have a strong radiative impact (Bretherton

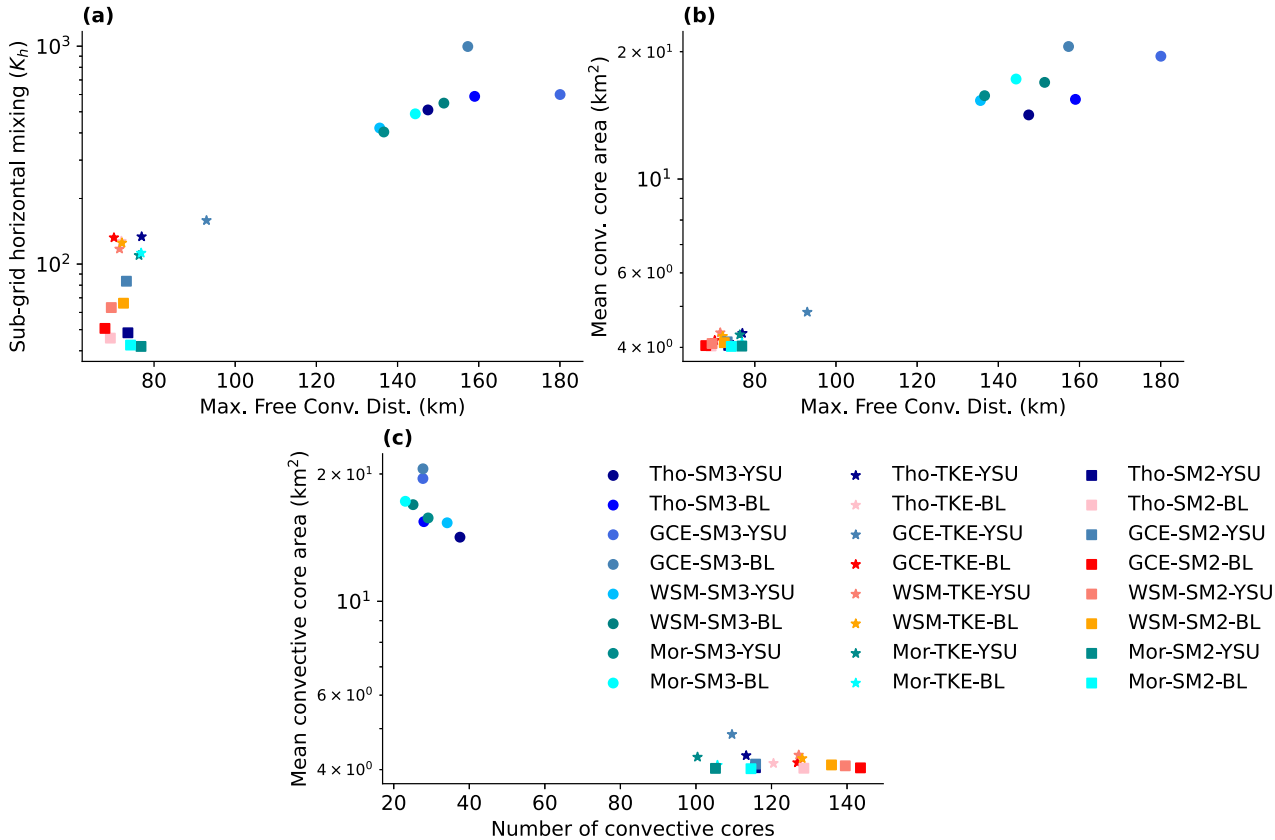

Figure 7. (a) Horizontal mixing (K_h) mean (from day 2 to 5) inside convective cores as a function of mean d_{clr} (from day 2 to 5), notice that the y-axis has a log scale, (b) mean convective core area as a function of mean d_{clr} (from day 2 to 5) and (c) mean convective core area (from day 2 to 5) as a function of mean number of convective cores (from day 2 to 5). Each plot includes Smag3 (circles), Smag2 (squares), and TKE (stars) simulations. Blue-green colors indicate runs that produce SA, while red-yellow colors represent runs without SA. The analysis excludes the first 48 hr for model spin-up.

et al., 2005). Thus one might expect ice sedimentation rates, through their impact on high anvil cloud cover to impact SA. Similarly, low cloud radiative forcing has also been attributed to have a strong role in aggregation occurrence, through their cloud-top radiative cooling (C. Muller & Held, 2012).

Another potential sensitivity to microphysics may involve the impact on cold pools. There have been numerous studies that have curtailed CP activity by the suppression of rainfall evaporation, and these have generally shown faster and stronger aggregation (Jeevanjee & Romps, 2013; C. Muller & Bony, 2015; Hwong & Muller, 2024). Cold pool arrangement and size is critical for SA (Haerter, 2019; Haerter et al., 2019; Nissen & Haerter, 2021), and this is through the triggering of convection from dynamical CP frontal lifting as well as a thermodynamic triggering role via the formation and advection of high humidity and MSE at the CP boundary, referred to as moisture rings (Tompkins, 2001). Thus microphysics schemes can potentially control the number of cores (e.g., Han et al., 2013; Weverberg et al., 2013) and *ergo* d_{clr} through cold pool properties.

In our simulations, sensitivity experiments increasing (Tho-SM2-BDI) and decreasing (Tho-SM2-YHI) the ice/snow fall speed on Tho-SM2-YSU and Tho-SM2-BL simulations had limited impact on the occurrence and timing of SA (Figure 3), perhaps somewhat unexpected given the past emphasis on LW-cloud feedbacks for forcing SA. The Tho-SM2-YHI experiment only delayed the aggregation onset by ≈3 days compare to Tho-SM2-YSU simulation, consistent with Bretherton et al. (2005).

In contrast to the fall speed experiments, changing the evaporation of rain to affect CPs has a stronger impact on SA. One explanation for this could be that changing CP intensities (Figures 8a and 8b and Figure S8 in Supporting Information S1) produces larger CPs (Figure 8e) which disfavors SA. Larger CPs increase cold pool to cold pool interaction since they are more space-filling (Haerter, 2019; Nissen & Haerter, 2021, see also Figure 8d), and enhance convective triggering at their gust fronts (e.g., Jeevanjee & Romps, 2013; Yanase et al., 2020). When the

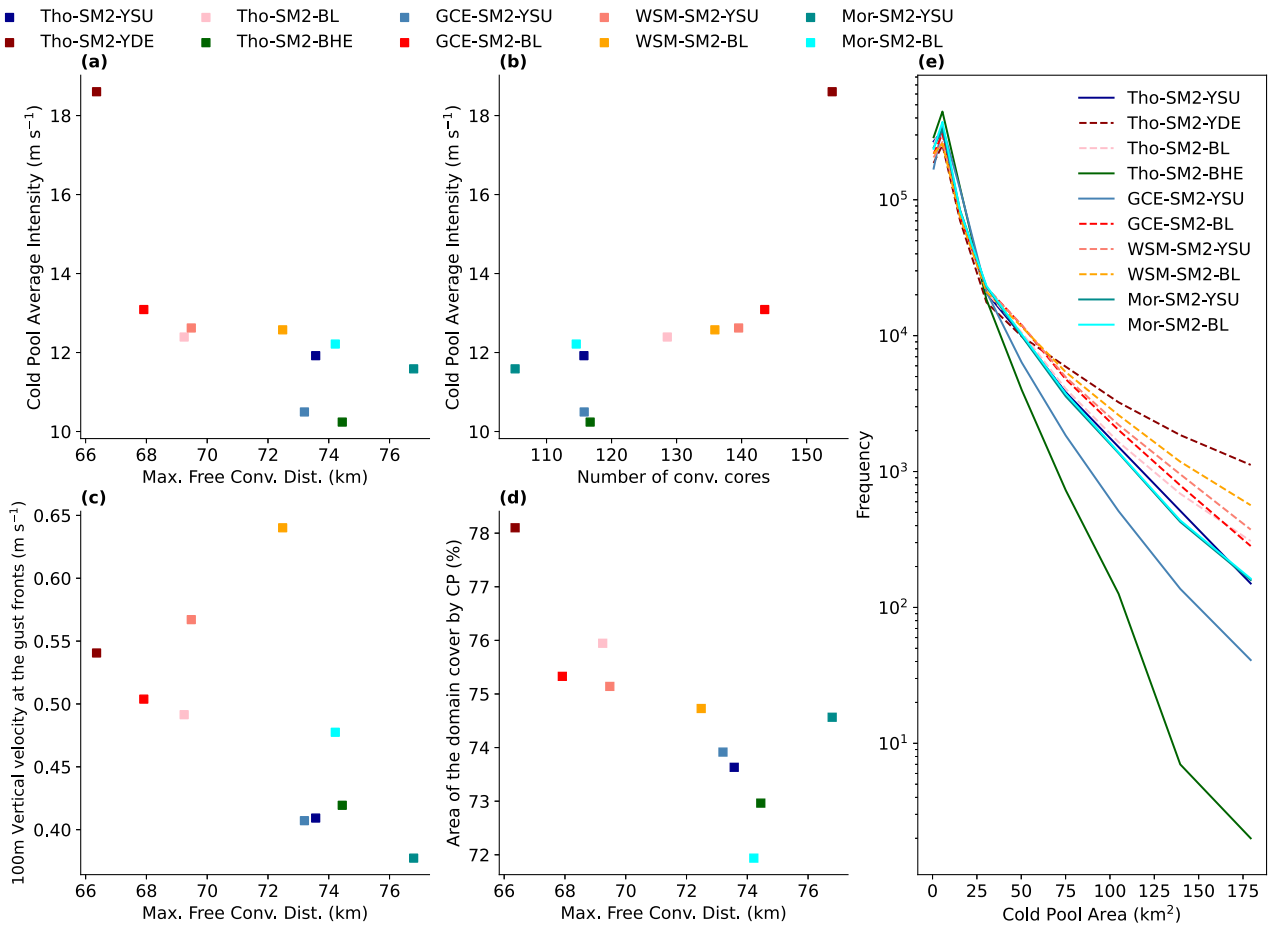

Figure 8. Cold pool average intensity (from day 2 to 5) as a function of (a) mean d_{clr}, and (b) number of convective cores. (c) Mean vertical velocity at 100 m (w_{100}) at the gust fronts of the CPs as a function of mean d_{clr} (from day 2 to 5). (d) Mean percentage area of the domain cover by the CPs as a function of mean d_{clr} (from day 2 to 5). (e) Frequency of cold pool area between day 2 to 5. For simulations using Smag2. Continuous lines depicted aggregated runs, meanwhile dashed lines show runs with random convection. Blue-green colors indicate runs that produce SA, meanwhile red-yellow colors represent runs without SA.

rainfall evaporation is modified (Tho-SM2-YDE and Tho-SM2-BHE) an analysis of the CP intensity (Figures 8a and 8b and Figure S8 in Supporting Information S1) reveals a clear trend: simulations that disallow the onset of SA tend to feature stronger CP intensities (Figures 8a and 8b), space filling CPs (Figure 8d), and a larger number of large CPs (Figure 8e), consistent with our earlier discussions.

In experiments with SA, CPs exhibit lesser strength and smaller size, accompanied by reduced convergence at their associated gust fronts (Figure 8). This reduced convergence (w_{100}) at CP gust fronts (Figure 8c) leads to a lower convective triggering rate (Casallas et al., 2023; Dawson et al., 2010; Fuglestvedt & Haerter, 2020; Li et al., 2015; Sherwood et al., 2010; Stevens, 2005; Tompkins, 2001), and subsequently to a decreased number of convective cores (resulting in larger d_{clr}) that favors the development of SA.

Fuglestvedt and Haerter (2020) highlighted the role of CP fronts in fostering a conducive environment for convection initiation by generating moist patches through convergence at their gusts (Schlemmer & Hohenegger, 2014; Tompkins, 2001). When these moist gust fronts collide, they trigger new convection (Tompkins, 2001). This underscores the significance of both convergence and the area/intensity of CPs in influencing convective triggering. Moreover, these gust fronts induce potent and sustained vertical velocities at the surface, fostering the initiation and intensification of convection (Böing et al., 2012). These insights shed light on why experiments using Mor's scheme consistently result in SA, while those employing the WSM scheme tend to remain random. Mor's scheme generates weaker and smaller CPs with limited convergence at their gust fronts, whereas the WSM scheme produces stronger and larger CPs with substantial convergence (Figure 8c, Figures S9 and S10 in Supporting Information S1), probably due to the fact that WSM simulations generate more

graupel (Figure S11 in Supporting Information S1). Graupel particles generally have higher fall speeds, enabling them to reach the melting layer more quickly. This contributes to increased rainfall, with greater rain evaporation, leading to larger CPs. This disparity leads to three critical outcomes: less efficient moisture redistribution, reduced area filled by CPs, and a smaller edge convergence (Figure 8d), favoring the development of dry regions in simulations with SA. In summary, varying CP strength alters d_{clr}, which can favor or hinder the development of SA.

These findings are supported by the evaporation of rain experiments. Tho-SM2-YDE, featuring increased CP area/intensity and gust front convergence, does not lead to SA (unlike Tho-SM2-YSU that develops SA). Conversely, Tho-SM2-BHE, with decreased CP area/intensity and gust front convergence, exhibits SA (unlike Tho-SM2-BL that does not develop SA).

4.3. Sensitivity to the PBL Mixing Scheme

Sensitivity of the occurrence of SA to the PBL mixing scheme choice was only seen when employing the Tho and GCE microphysics schemes (Figures 9a and 9b). Simulations employing the YSU scheme (non-local) have fewer cores, and increased core distances compared to those using the BouLac scheme (local).

How can the choice of PBL scheme influence core count and spacing? Hu et al. (2010) demonstrated that non-local schemes enhance vertical mixing, particularly at cloud tops, increasing entrainment and resulting in a warmer, drier boundary layer. This effect is evident in our results as well. Figure 9 highlights the anomaly (difference) in water vapor between the Smag2 simulations using YSU and BL schemes before SA starts to develop. The figure shows that, across much of the boundary layer, the YSU simulations exhibit drier conditions (red colors) compared to their BL counterparts. This drying of the boundary layer significantly impacts the distribution of convective inhibition (CIN), as illustrated in Figure 10 and Figure S12 in Supporting Information S1 in which the mass flux is depicted. Figure 10 presents the probability density function (PDF) of CIN values for the Smag2 simulations, with red lines representing simulations without SA and blue lines indicating those that develop SA. Simulations employing the non-local YSU scheme exhibit a notable shift toward higher CIN values overall, compared to the local BL schemes (Figure 10). This shift reduces the area with sufficiently low CIN values needed to trigger convection (Behrendt et al., 2011, vertical dotted line in Figure 10). As a result, simulations using the YSU scheme tend to have fewer but more active convective cores (Figure S12 in Supporting Information S1) and a larger d_{clr}.

In addition to the aforementioned, non-local schemes result in significantly higher low cloud amounts compared to local schemes, nearly doubling the low cloud fraction in our simulations. These low clouds enhance radiative cooling, balanced by stronger subsidence, which increase the area affected by large CIN values, thereby hindering convective triggering, reducing core counts, and increasing d_{clr}. To investigate this, we conducted a 20-day simulation (Table S3 in Supporting Information S1) named Tho-SM2-YNL, in which we excluded low-level clouds from the longwave cooling calculation by zeroing the liquid condensates at each time step and height (Coppin & Bony, 2015; C. Muller & Held, 2012; C. Muller & Bony, 2015). In doing so, we effectively tested the role of low clouds in SA by examining how the absence of their cooling and associated feedbacks would impact the system. However, this simulation did not develop SA, and its CIN values were more akin to those observed in the Tho-SM2-BL simulation, rather than the Tho-SM2-YSU run, with large areas of strong CIN (Figure 10a).

This outcome suggests that non-local PBL schemes, by promoting the presence of low clouds in dry regions, induce enhanced subsidence and subsequent increase in CIN due to the radiative cooling from those clouds. This, in turn, generates a positive feedback on the d_{clr} metric, further drying the areas between convective cores through increased radiative cooling and subsidence. However, the effects of low clouds in the simulations are intertwined with other factors in the simulation, making it difficult to isolate their impact.

In summary, non-local schemes simulate a larger low cloud fraction, which enhances subsidence and promotes SA (C. Muller & Held, 2012). Furthermore, these schemes increase vertical mixing, leading to greater entrainment and higher cloud tops (Hu et al., 2010). This creates a warmer and drier environment, alters the distribution of CIN, reduces convective triggering, increases d_{clr}, and further supports SA.

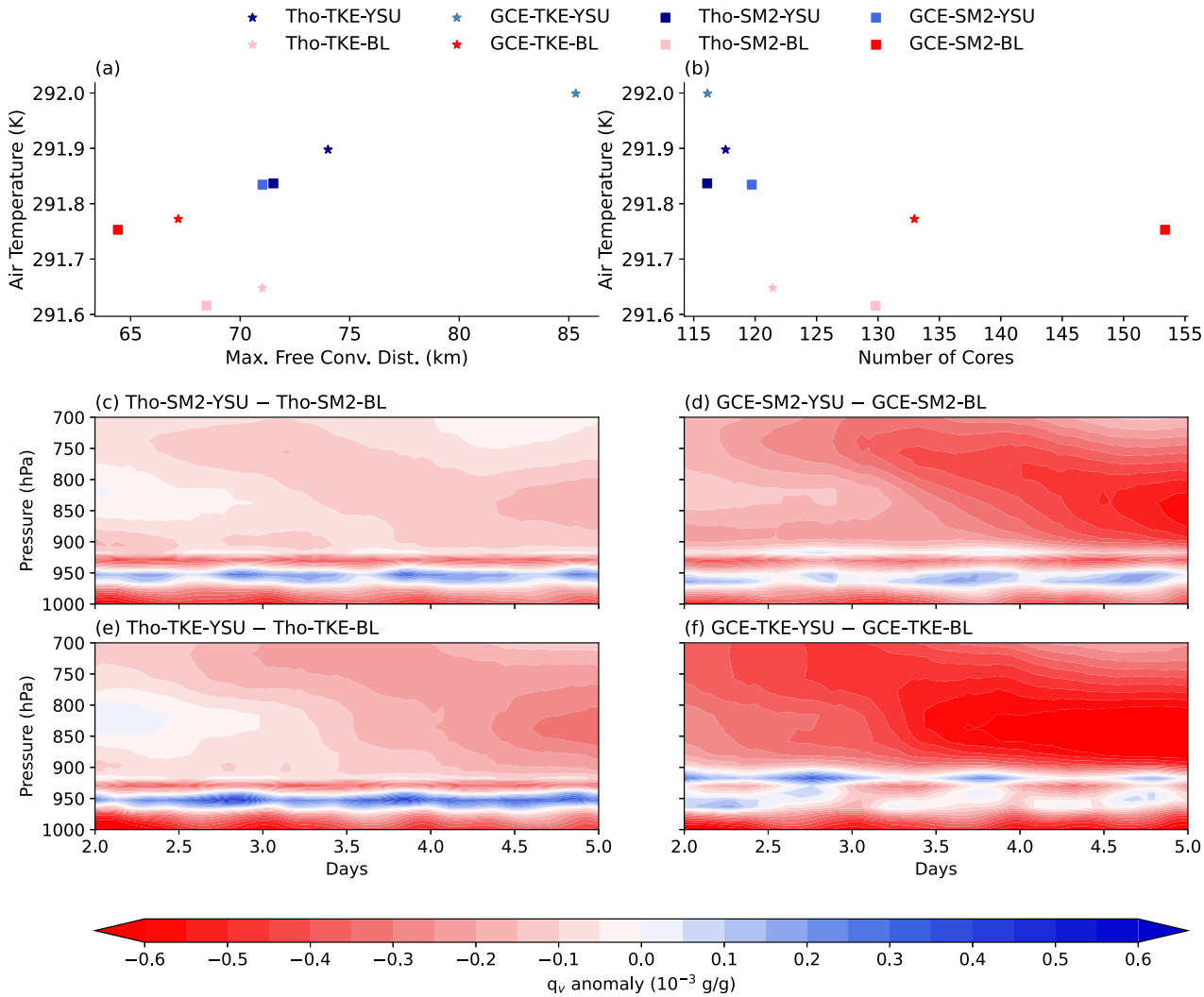

Figure 9. Mean air temperature between day 2 and 5 in the boundary layer, plotted as function of (a) mean d_{clr} and (b) mean number of convection cores between day 2 and 5. Blue-green colors indicate runs that produce SA, meanwhile red-yellow colors represent runs without SA. Water vapor mixing ratio anomaly evolution (colors) in the boundary layer for (c) Tho-SM2-YSU − Tho-SM2-BL, (d) GCE-SM2-YSU − GCE-SM2-BL, (e) Tho-TKE-YSU − Tho-TKE-BL, and (f) GCE-TKE-YSU − GCE-TKE-BL between day 2 and day 5 (pre-onset of SA).

5. Conclusions

The aim of this study was to evaluate the hypothesis of Biagioli and Tompkins (2023) that the occurrence of deep convective self-aggregation depends on the convective spacing, as expressed through the convective free distance d_{clr} measured in early, pre-onset phase of simulations. The argument was that a larger inter-convective distance leads to a greater horizontal variability in water vapor, which if exceeding a critical threshold could tip the simulation into an aggregated state. This hypothesis was tested using a large perturbed physics ensemble of idealized radiative-convective equilibrium simulations using the WRF model.

We examined 24 different combinations of three key parameterization schemes: those governing sub-grid scale horizontal mixing, vertical mixing through various planetary boundary layer (PBL) schemes (which also affect local vertical mixing in the free troposphere in some cases), and microphysics parameterizations. Our analysis highlights the critical role of the spacing between deep convective updrafts during the initial "random" simulation stage, as measured by d_{clr}. In simulations with large d_{clr}, the extensive dry regions between convective cores experience prevailing subsidence, which promotes the well-known self-aggregation feedbacks. A large d_{clr} provides the initial conditions for the formation and intensification of a dry area. Once established, SA feedbacks can further strengthen this dry area through radiatively induced subsidence drying. Therefore, the convective

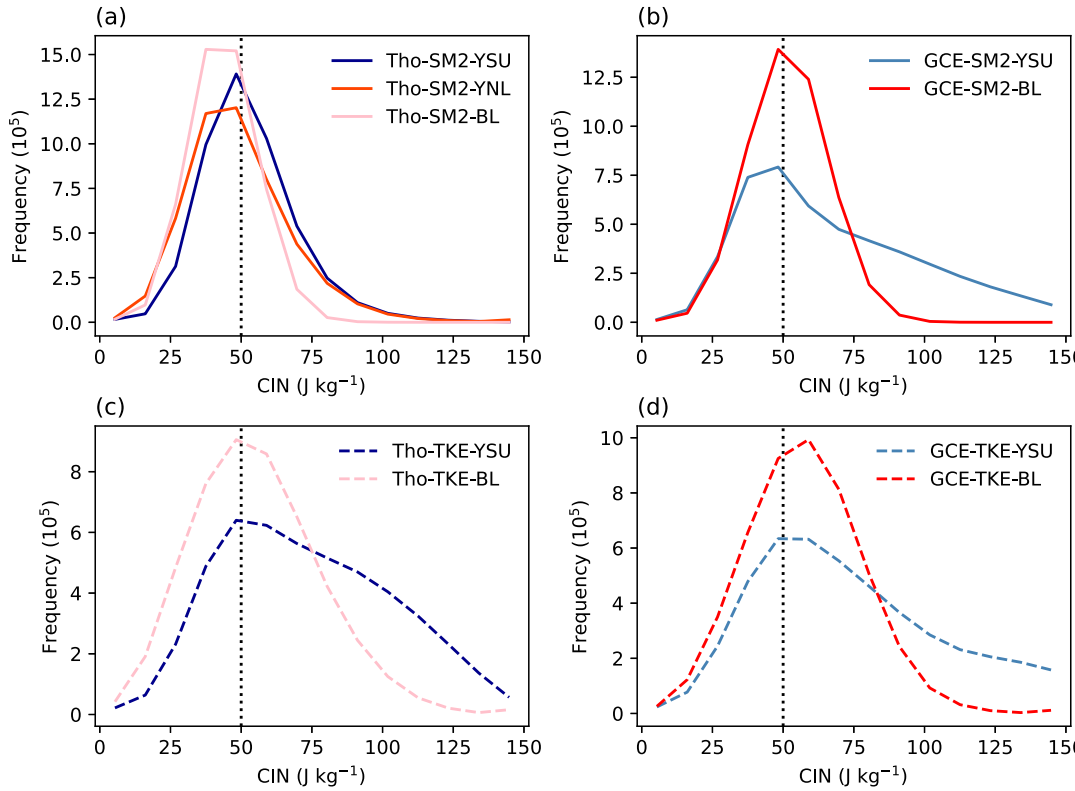

Figure 10. PDFs for convective inhibition (CIN) for (a) Tho-SM2-YSU, Tho-SM2-BL, and Tho-SM2-YNL, (b) GCE-SM2-YSU and GCE-SM2-BL, (c) Tho-TKE-YSU and Tho-TKE-BL, and (d) GCE-TKE-YSU and GCE-TKE-BL from day 2 to day 5. The vertical dotted line indicates the threshold identified by Behrendt et al. (2011) beyond which deep convection is strongly disfavor. Notice that blue colors depict aggregated runs, while red colors represent runs without SA.

arrangement of any model configuration in the early simulation days, as indicated by d_{clr}, can predict whether the simulation will transition to an SA state after 10–30 days or maintain a random configuration.

All three schemes impact the mean convective spacing. The horizontal mixing coefficient was found to greatly impact the mean core size of convective updrafts, with some schemes producing fewer, far wider towers, which thus lead to aggregation. We emphasize that this represents a re-interpretation of the results of Tompkins and Semie (2017), who attributed the sensitivity of SA to horizontal mixing to the role of updraft entrainment, and is also consistent with the results of Silvestri et al. (2024).

The microphysics schemes impacted d_{clr} and thus SA through the influence on the cold pool dynamics. Schemes that generate larger, more vigorous cold pools tend to have smaller convective free areas. In these cases the cold-pools are more "space-filling" to adopt the nomenclature of Nissen and Haerter (2021), cold pools trigger convection at their edge and redistribute moisture more efficiently to dry regions (Jeevanjee & Romps, 2013). Somewhat surprisingly, given that much previous work on SA has emphasized the key role of LW-cloud feedback on initiating SA, perturbations to ice fall speeds had a limited impact on SA.

The vertical mixing scheme also influenced the boundary layer. Non-local schemes produced stronger vertical mixing and entrainment at the PBL top resulted in warmer and drier boundary layers on average. This significantly impacted the distribution of CIN, leading to fewer and more widely spaced deep convective updrafts. Consequently, these non-local schemes were more likely to lead to SA, compare to the local schemes, all else being equal.

The perturbed physics ensemble has confirmed one tenant of Biagioli and Tompkins (2023), namely that the spacing between deep convective towers in the pre-aggregation phase as measured by d_{clr} is key to the eventual onset of convective self-aggregation. However, Biagioli and Tompkins (2023) went further to combine a theoretical estimate of d_{clr} that incorporated the model domain size and resolution together with other idealized

parameters that described how convection was sensitive to water vapor, and how local convective moistening was subsequently communicated across the domain. This parameter combination was designated the aggregation number (N_{ag}), which was able to predict SA occurrence in their idealized stochastic model simulations. The next step would be to attempt to derive estimates of these parameters from the perturbed physics ensemble, or other ensemble RCE experiments such as RCEMIP, and thus estimate N_{ag} or a variant of N_{ag} from full physics models.

Data Availability Statement

The data presented in this paper are available on Figshare (Casallas, 2024a), and all software used in this research has been publicly released on GitHub (Casallas, 2025).

Acknowledgments
This article is based on chapter 3 of AC Ph.D. thesis. The authors thank Graziano Giuliani for his coding assistance. We also thank Daniel Hernández-Deckers, Paolina Cerlini, and especially to Giovanni Biagioli for discussions and feedback. We also thank two reviewers for their insightful comments. AC was supported by a fellowship awarded by ICTP and by the European Union Horizon 2020 Marie Skłodowska-Curie grant agreement No. 101034413. CM acknowledges funding from the European Research Council (ERC) under the European Union's Horizon 2020 research and innovation program (Project CLUSTER, Grant Agreement No. 805041).

References

Abramian, S., Muller, C., & Risi, C. (2022). Shear-convection interactions and orientation of tropical squall lines. *Geophysical Research Letters*, *49*(1), e2021GL095184. https://doi.org/10.1029/2021GL095184

Bao, J., & Sherwood, S. C. (2019). The role of convective self-aggregation in extreme instantaneous versus daily precipitation. *Journal of Advances in Modeling Earth Systems*, *11*(1), 19–33. https://doi.org/10.1029/2018MS001503

Becker, T., & Wing, A. A. (2020). Understanding the extreme spread in climate sensitivity within the radiative-convective equilibrium model intercomparison project. *Journal of Advances in Modeling Earth Systems*, *12*(10), e2020MS002165. https://doi.org/10.1029/2020MS002165

Behrendt, A., Pal, S., Aoshima, F., Bender, M., Blyth, A., Corsmeier, U., et al. (2011). Observation of convection initiation processes with a suite of state-of-the-art research instruments during COPS IOP 8b. *Quarterly Journal of the Royal Meteorological Society*, *137*(S1), 81–100. https://doi.org/10.1002/qj.758

Benjamin, T. B. (1968). Gravity currents and related phenomena. *Journal of Fluid Mechanics*, *31*(2), 209–248. https://doi.org/10.1017/S0022112068000133

Beucler, T., Leutwyler, D., & Windmiller, J. M. (2020). Quantifying convective aggregation using the tropical moist margin's length. *Journal of Advances in Modeling Earth Systems*, *12*(10), e2020MS002092. https://doi.org/10.1029/2020MS002092

Biagioli, G., & Tompkins, A. (2023). A dimensionless parameter for predicting convective self-aggregation onset in a stochastic reaction-diffusion model of tropical radiative-convective equilibrium. *Journal of Advances in Modeling Earth Systems*, *15*(5), e2022MS003231. https://doi.org/10.1029/2022MS003231

Böing, S., Jonker, H., Siebesma, A., & Grabowski, W. (2012). Influence of the subcloud layer on the development of a deep convective ensemble. *Journal of the Atmospheric Sciences*, *69*(9), 2682–2698. https://doi.org/10.1175/JAS-D-11-0317.1

Bougeault, P., & Lacarrere, P. (1989). Parameterization of orography-induced turbulence in a mesobeta–scale model. *Monthly Weather Review*, *117*(8), 1872–1890. https://doi.org/10.1175/1520-0493(1989)117⟨1872:POOITI⟩2.0.CO;2

Bretherton, C., Blossey, P., & Khairoutdinov, M. (2005). An energy-balance analysis of deep convective self-aggregation above uniform SST. *Journal of the Atmospheric Sciences*, *62*(12), 4273–4292. https://doi.org/10.1175/JAS3614.1

Bretherton, C., Peters, M., & Back, L. (2004). Relationships between water vapor path and precipitation over the tropical oceans. *Journal of Climate*, *17*(7), 1517–1528. https://doi.org/10.1175/1520-0442(2004)017⟨1517:RBWVPA⟩2.0.CO;2

Casallas, A. (2024a). Idealized_mp_pbl_tke_sm.zip [Dataset]. *Figshare*. https://doi.org/10.6084/m9.figshare.27291468.v1

Casallas, A. (2024b). *Understanding convective organization and seeking it through observations* (Unpublished doctoral dissertation). Università degli Studi di Trieste. Retrieved from https://hdl.handle.net/11368/3076620

Casallas, A. (2025). d_clr_sensitivity_james_2025 [Software]. *GitHub*. Retrieved from https://github.com/Casicus94/d_clr_sensitivity_JAMES_2025

Casallas, A., Cabrera, A., Guevara-Luna, M., Tompkins, A., Gonzalez, Y., Aranda, J., et al. (2024). Air pollution analysis in northwestern south America: A new Lagrangian framework. *Science of the Total Environment*, *906*, 167350. https://doi.org/10.1016/j.scitotenv.2023.167350

Casallas, A., Hernández-Deckers, D., & Mora-Páez, H. (2023). Understanding convective storms in a tropical, high-altitude location with in-situ meteorological observations and GPS-derived water vapor. *Atmósfera*, *36*(2), 225–238. https://doi.org/10.20937/ATM.53051

Cerlini, P. B., Saraceni, M., & Silvestri, L. (2023). Competing effect of radiative and moisture feedback in convective aggregation states in two CRMS. *Journal of Advances in Modeling Earth Systems*, *15*(2), e2022MS003323. https://doi.org/10.1029/2022MS003323

Cohen, B. G., & Craig, G. C. (2004). The response time of a convective cloud ensemble to a change in forcing. *Quarterly Journal of the Royal Meteorological Society*, *130*(598), 933–944. https://doi.org/10.1256/qj.02.218

Cohen, B. G., & Craig, G. C. (2006). Fluctuations in an equilibrium convective ensemble. Part II: Numerical experiments. *Journal of the Atmospheric Sciences*, *63*(8), 2005–2015. https://doi.org/10.1175/JAS3710.1

Coppin, D., & Bony, S. (2015). Physical mechanisms controlling the initiation of convective self-aggregation in a general circulation model. *Journal of Advances in Modeling Earth Systems*, *7*(4), 2060–2078. https://doi.org/10.1002/2015MS000571

Craig, G. C., & Mack, J. M. (2013). A coarsening model for self-organization of tropical convection. *Journal of Geophysical Research: Atmospheres*, *118*(16), 8761–8769. https://doi.org/10.1002/jgrd.50674

Da Silva, N. A., Muller, C., Shamekh, S., & Fildier, B. (2021). Significant amplification of instantaneous extreme precipitation with convective self-aggregation. *Journal of Advances in Modeling Earth Systems*, *13*(11), e2021MS002607. https://doi.org/10.1029/2021MS002607

Dawson, D. T., Xue, M., Milbrandt, J. A., & Yau, M. K. (2010). Comparison of evaporation and cold pool development between single-moment and multimoment bulk microphysics schemes in idealized simulations of tornadic thunderstorms. *Monthly Weather Review*, *138*(4), 1152–1171. https://doi.org/10.1175/2009MWR2956.1

Drager, A. J., & van den Heever, S. C. (2017). Characterizing convective cold pools. *Journal of Advances in Modeling Earth Systems*, *9*(3), 1091–1115. https://doi.org/10.1002/2016MS000788

Dudhia, J. (1989). Numerical study of convection observed during the winter monsoon experiment using a mesoscale two-dimensional model. *Journal of the Atmospheric Sciences*, *46*(20), 3077–3107. https://doi.org/10.1175/1520-0469(1989)046⟨3077:NSOCOD⟩2.0.CO;2

Dudhia, J., Hong, S.-Y., & Lim, K.-S. (2008). A new method for representing mixed-phase particle fall speeds in bulk microphysics parameterizations. *Journal of the Meteorological Society of Japan*, *86*(1), 33–44. https://doi.org/10.2151/jmsj.86a.33

Emanuel, K., Wing, A. A., & Vincent, E. M. (2014). Radiative-convective instability. *Journal of Advances in Modeling Earth Systems*, *6*(1), 75–90. https://doi.org/10.1002/2013ms000270

Field, P. R., Heymsfield, A. J., & Bansemer, A. (2007). Snow size distribution parameterization for midlatitude and tropical ice clouds. *Journal of the Atmospheric Sciences*, *64*(12), 4346–4365. https://doi.org/10.1175/2007JAS2344.1

Fuglestvedt, H. F., & Haerter, J. O. (2020). Cold pools as conveyor belts of moisture. *Geophysical Research Letters*, *47*(12), e2020GL087319. https://doi.org/10.1029/2020GL087319

Grabowski, W. W., & Moncrieff, M. W. (2004). Moisture–convection feedback in the tropics. *Quarterly Journal of the Royal Meteorological Society*, *130*(604), 3081–3104. https://doi.org/10.1256/qj.03.135

Grant, L. D., & van den Heever, S. C. (2016). Cold pool dissipation. *Journal of Geophysical Research: Atmospheres*, *121*(3), 1138–1155. https://doi.org/10.1002/2015JD023813

Grant, L. D., & van den Heever, S. C. (2018). Cold pool-land surface interactions in a dry continental environment. *Journal of Advances in Modeling Earth Systems*, *10*(7), 1513–1526. https://doi.org/10.1029/2018MS001323

Haerter, J. O. (2019). Convective self-aggregation as a cold pool-driven critical phenomenon. *Geophysical Research Letters*, *46*(7), 4017–4028. https://doi.org/10.1029/2018GL081817

Haerter, J. O., Böing, S. J., Henneberg, O., & Nissen, S. B. (2019). Circling in on convective organization. *Geophysical Research Letters*, *46*(12), 7024–7034. https://doi.org/10.1029/2019GL082092

Han, M., Braun, S. A., Matsui, T., & Williams, C. R. (2013). Evaluation of cloud microphysics schemes in simulations of a winter storm using radar and radiometer measurements. *Journal of Geophysical Research: Atmospheres*, *118*(3), 1401–1419. https://doi.org/10.1002/jgrd.50115

Held, I., Hemler, R., & Ramaswamy, V. (1993). Radiative-convective equilibrium with explicit two-dimensional moist convection. *Journal of the Atmospheric Sciences*, *50*(23), 3909–3927. https://doi.org/10.1175/1520-0469(1993)050⟨3909:RCEWET⟩2.0.CO;2

Hohenegger, C., & Stevens, B. (2016). Coupled radiative convective equilibrium simulations with explicit and parameterized convection. *Journal of Advances in Modeling Earth Systems*, *8*(3), 1468–1482. https://doi.org/10.1002/2016MS000666

Hohenegger, C., & Stevens, B. (2018). The role of the permanent wilting point in controlling the spatial distribution of precipitation. *Proceedings of the National Academy of Sciences of the United States of America*, *115*(22), 5692–5697. https://doi.org/10.1073/pnas.1718842115

Holloway, C. E. (2017). Convective aggregation in realistic convective-scale simulations. *Journal of Advances in Modeling Earth Systems*, *9*(2), 1450–1472. https://doi.org/10.1002/2017MS000980

Holloway, C. E., & Woolnough, S. J. (2016). The sensitivity of convective aggregation to diabatic processes in idealized radiative-convective equilibrium simulations. *Journal of Advances in Modeling Earth Systems*, *8*(1), 166–195. https://doi.org/10.1002/2015MS000511

Hong, S., Dudhia, J., & Chen, S. (2004). A revised approach to ice microphysical processes for the bulk parameterization of clouds and precipitation. *Monthly Weather Review*, *132*(1), 103–120. https://doi.org/10.1175/1520-0493(2004)132⟨0103:ARATIM⟩2.0.CO;2

Hong, S., & Lim, J. (2006). The WRF single-moment 6-class microphysics scheme (WSM6). *Asia-pacific Journal of Atmospheric Sciences*, *42*, 129–151.

Hong, S., Noh, Y., & Dudhia, J. (2006). A new vertical diffusion package with an explicit treatment of entrainment processes. *Monthly Weather Review*, *134*(9), 2318–2341. https://doi.org/10.1175/MWR3199.1

Hong, S., & Pan, H. (1996). Nonlocal boundary layer vertical diffusion in a medium-range forecast model. *Monthly Weather Review*, *124*(10), 2322–2339. https://doi.org/10.1175/1520-0493(1996)124⟨2322:NBLVDI⟩2.0.CO;2

Hu, X., Nielsen-Gammon, J., & Zhang, F. (2010). Evaluation of three planetary boundary layer schemes in the WRF model. *Journal of Applied Meteorology and Climatology*, *49*(9), 1831–1844. https://doi.org/10.1175/2010JAMC2432.1

Huang, J.-D., & Wu, C.-M. (2022). A framework to evaluate convective aggregation: Examples with different microphysics schemes. *Journal of Geophysical Research: Atmospheres*, *127*(5), e2021JD035886. https://doi.org/10.1029/2021JD035886

Hwong, Y.-L., & Muller, C. J. (2024). The unreasonable efficiency of total rain evaporation removal in triggering convective self-aggregation. *Geophysical Research Letters*, *51*(6), e2023GL106523. https://doi.org/10.1029/2023GL106523

Iacono, M., Delamere, J., Mlawer, E., Shephard, M., Clough, S., & Collins, D. (2008). Radiative forcing by long-lived greenhouse gases: Calculations with the AER radiative transfer models. *Journal of Geophysical Research*, *113*(D13). https://doi.org/10.1029/2008JD009944

Iverson, E., Thompson, G., & Nygaard, B. (2021). Improvements to melting snow behavior in a bulk microphysics scheme. *Atmospheric Research*, *253*, 105471. https://doi.org/10.1016/j.atmosres.2021.1054711

Jeevanjee, N., & Romps, D. M. (2013). Convective self-aggregation, cold pools, and domain size. *Geophysical Research Letters*, *40*(5), 994–998. https://doi.org/10.1002/grl.50204

Jordan, C. (1958). Mean soundings for the west indies area. *Journal of the Atmospheric Sciences*, *15*(1), 91–97. https://doi.org/10.1175/1520-0469(1958)015⟨0091:MSFTWI⟩2.0.CO;2

Lang, S., Tao, W., Chern, J., Wu, D., & Li, X. (2014). Benefits of a fourth ice class in the simulated radar reflectivities of convective systems using a bulk microphysics scheme. *Journal of the Atmospheric Sciences*, *71*(10), 3583–3612. https://doi.org/10.1175/JAS-D-13-0330.1

Li, Z., Zuidema, P., Zhu, P., & Morrison, H. (2015). The sensitivity of simulated shallow cumulus convection and cold pools to microphysics. *Journal of the Atmospheric Sciences*, *72*(9), 3340–3355. https://doi.org/10.1175/JAS-D-14-0099.1

Lin, Y., RD Farley, R., & Orville, H. (1983). Bulk parameterization of the snow field in a cloud model. *Journal of Applied Meteorology and Climatology*, *22*(6), 1065–1092. https://doi.org/10.1175/1520-0450(1983)022⟨1065:BPOTSF⟩2.0.CO;2

Maneewongvatana, S., & Mount, D. M. (1999). Analysis of approximate nearest neighbor searching with clustered point sets. Retrieved from https://arxiv.org/abs/cs/9901013

Mapes, B. (2001). Water's two height scales: The moist adiabat and the radiative troposphere. *Quarterly Journal of the Royal Meteorological Society*, *127*(577), 2353–2366. https://doi.org/10.1002/qj.49712757708

Martin, G. M., Johnson, D. W., & Spice, A. (1994). The measurement and parameterization of effective radius of droplets in warm stratocumulus clouds. *Journal of the Atmospheric Sciences*, *51*(13), 1823–1842. https://doi.org/10.1175/1520-0469(1994)051⟨1823:TMAPOE⟩2.0.CO;2

Mauritsen, T., & Stevens, B. (2015). Missing iris effect as a possible cause of muted hydrological change and high climate sensitivity in models. *Nature Geoscience*, *8*(5), 346–351. https://doi.org/10.1038/ngeo2414

Mlawer, E. J., Taubman, S. J., Brown, P. D., Iacono, M. J., & Clough, S. A. (1997). Radiative transfer for inhomogeneous atmospheres: RRTM, a validated correlated-k model for the longwave. *Journal of Geophysical Research*, *102*(D14), 16663–16682. https://doi.org/10.1029/97JD00237

Monin, A., & Obukhov, A. (1954). Basic laws of turbulent mixing in the surface layer of the atmosphere. *Trudy Akademii Nauk SSSR, Geofizicheskiy Institut*, *24*(151), 163–187.

Morrison, H., Curry, J., & Khvorostyanov, V. (2005). A new double-moment microphysics parameterization for application in cloud and climate models. Part I: Description. *Journal of the Atmospheric Sciences*, *62*(6), 1665–1677. https://doi.org/10.1175/JAS3446.1

Morrison, H., & Gettelman, A. (2008). A new two-moment bulk stratiform cloud microphysics scheme in the community atmosphere model, version 3 (CAM3). Part I: Description and numerical tests. *Journal of Climate*, *21*(15), 3642–3659. https://doi.org/10.1175/2008JCLI2105.1

Morrison, H., & Pinto, J. (2006). Intercomparison of bulk cloud microphysics schemes in mesoscale simulations of springtime Arctic mixed-phase stratiform clouds. *Monthly Weather Review*, *134*(7), 1880–1900. https://doi.org/10.1175/MWR3154.1

Muller, C., & Bony, S. (2015). What favors convective aggregation and why? *Geophysical Research Letters*, *42*(13), 5626–5634. https://doi.org/10.1002/2015GL064260

Muller, C., & Held, I. (2012). Detailed investigation of the self-aggregation of convection in cloud-resolving simulations. *Journal of the Atmospheric Sciences*, *69*(8), 2551–2565. https://doi.org/10.1175/JAS-D-11-0257.1

Muller, C., Yang, D., Craig, G., Cronin, T., Fildier, B., Haerter, J. O., et al. (2022). Spontaneous aggregation of convective storms. *Annual Review of Fluid Mechanics*, *54*(1), 133–157. https://doi.org/10.1146/annurev-fluid-022421-011319

Muller, S., Caillaud, C., Chan, S., de Vries, H., Bastin, S., Berthou, S., et al. (2022). Evaluation of alpine-mediterranean precipitation events in convection-permitting regional climate models using a set of tracking algorithms. *Climate Dynamics*, *61*(1–2), 939–957. https://doi.org/10.1007/s00382-022-06555-z

Müller, S. K., & Hohenegger, C. (2020). Self-aggregation of convection in spatially varying sea surface temperatures. *Journal of Advances in Modeling Earth Systems*, *12*(1), e2019MS001698. https://doi.org/10.1029/2019MS001698

Naumann, A., Stevens, B., & Hohenegger, C. (2019). A moist conceptual model for the boundary layer structure and radiatively driven shallow circulations in the trades. *Journal of the Atmospheric Sciences*, *76*(5), 1289–1306. https://doi.org/10.1175/JAS-D-18-0226.1

Nissen, S. B., & Haerter, J. O. (2021). Circling in on convective self-aggregation. *Journal of Geophysical Research: Atmospheres*, *126*(20), e2021JD035331. https://doi.org/10.1029/2021JD035331

Noh, Y., Cheon, W., Hong, S.-Y., & Raasch, S. (2003). Improvement of the K-profile model for the planetary boundary layer based on large eddy simulation data. *Boundary-Layer Meteorology*, *107*(2), 401–427. https://doi.org/10.1023/A:1022146015946

Potvin, C., Skinner, P., Hoogewind, K., Coniglio, M., Gibbs, J., Clark, A., et al. (2020). Assessing systematic impacts of PBL schemes on storm evolution in the NOAA warn-on-forecast system. *Monthly Weather Review*, *148*(6), 2567–2590. https://doi.org/10.1175/MWR-D-19-0389.1

Rushley, S. S., Kim, D., Bretherton, C. S., & Ahn, M.-S. (2018). Reexamining the nonlinear moisture-precipitation relationship over the tropical oceans. *Geophysical Research Letters*, *45*(2), 1133–1140. https://doi.org/10.1002/2017GL076296

Rutledge, S., & Hobbs, P. (1983). The mesoscale and microscale structure and organization of clouds and precipitation in midlatitude cyclones. VIII: A model for the "seeder-feeder" process in warm-frontal rainbands. *Journal of the Atmospheric Sciences*, *40*(5), 1185–1206. https://doi.org/10.1175/1520-0469(1983)040⟨1185:TMAMSA⟩2.0.CO;2

Schlemmer, L., & Hohenegger, C. (2014). The Formation of wider and deeper clouds as a result of cold-pool dynamics. *Journal of the Atmospheric Sciences*, *71*(8), 2842–2858. https://doi.org/10.1175/JAS-D-13-0170.1

Shamekh, S., Muller, C., Duvel, J.-P., & D'Andrea, F. (2020). Self-aggregation of convective clouds with interactive sea surface temperature. *Journal of Advances in Modeling Earth Systems*, *12*(11), e2020MS002164. https://doi.org/10.1029/2020MS002164

Sherwood, S. C., Roca, R., Weckwerth, T. M., & Andronova, N. G. (2010). Tropospheric water vapor, convection, and climate. *Reviews of Geophysics*, *48*(2). https://doi.org/10.1029/2009rg000301

Shi, X., & Fan, Y. (2021). Modulation of the bifurcation in radiative-convective equilibrium by gray-zone cloud and turbulence parameterizations. *Journal of Advances in Modeling Earth Systems*, *13*(10), e2021MS002632. https://doi.org/10.1029/2021MS002632

Silvestri, L., Saraceni, M., & Bongioannini Cerlini, P. (2024). Numerical diffusion and turbulent mixing in convective self-aggregation. *Journal of Advances in Modeling Earth Systems*, *16*(5), e2023MS004151. https://doi.org/10.1029/2023MS004151

Skamarock, W., Klemp, J., Dudhia, J., Gill, D., Liu, Z., Berner, J., et al. (2019). *A description of the advanced research WRF version 4* (Tech. Rep.). NCAR Technical Note NCAR/TN-556+STR. https://doi.org/10.5065/1dfh-6p97

Smagorinsky, J. (1963). General circulation experiments with the primitive equations: I. The basic experiment. *Monthly Weather Review*, *91*(3), 99–164. https://doi.org/10.1175/1520-0493(1963)091⟨0099:GCEWTP⟩2.3.CO;2

Sobel, A., Nilsson, J., & Polvani, L. (2001). The weak temperature gradient approximation and balanced tropical moisture waves. *Journal of the Atmospheric Sciences*, *58*(23), 3650–3665. https://doi.org/10.1175/1520-0469(2001)058⟨3650:TWTGAA⟩2.0.CO;2

Stephens, G., van den Heever, S., & Pakula, L. (2008). Radiative–convective feedbacks in idealized states of radiative–convective equilibrium. *Journal of the Atmospheric Sciences*, *65*(12), 3899–3916. https://doi.org/10.1175/2008JAS2524.1

Stevens, B. (2005). Atmospheric moist convection. *Annual Review of Earth and Planetary Sciences*, *33*(1), 605–643. https://doi.org/10.1146/annurev.earth.33.092203.122658

Stohl, A., Forster, C., Frank, A., Seibert, P., & Wotawa, G. (2005). Technical note: The Lagrangian particle dispersion model flexpart version 6.2. *Atmospheric Chemistry and Physics*, *5*(9), 2461–2474. https://doi.org/10.5194/acp-5-2461-2005

Tao, W., Lang, S., Zeng, X., Li, X., Matsui, T., Mohr, K., et al. (2014). The Goddard Cumulus Ensemble model (GCE): Improvements and applications for studying precipitation processes. *Atmospheric Research*, *143*, 392–424. https://doi.org/10.1016/j.atmosres.2014.03.005

Tao, W., & Simpson, J. (1993). Goddard Cumulus ensemble model. Part I: Model description. *Terrestrial, Atmospheric and Oceanic Sciences Journal*, *4*, 35–75. https://doi.org/10.1007/s00703-001-0594-7

Therry, G., & Lacarrère, P. (1983). Improving the Eddy Kinetic Energy model for planetary boundary layer description. *Monthly Weather Review*, *25*(1), 63–88. https://doi.org/10.1007/BF00122098

Thompson, G., Field, P. R., Rasmussen, R. M., & Hall, W. D. (2008). Explicit forecasts of winter precipitation using an improved bulk microphysics scheme. Part II: Implementation of a new snow parameterization. *Monthly Weather Review*, *136*(12), 5095–5115. https://doi.org/10.1175/2008MWR2387.1

Tompkins, A. (2001). Organization of tropical convection in low vertical wind shears: The role of cold pools. *Journal of the Atmospheric Sciences*, *58*(13), 1650–1672. https://doi.org/10.1175/1520-0469(2001)058⟨1650:OOTCIL⟩2.0.CO;2

Tompkins, A., & Craig, G. (1998). Radiative–convective equilibrium in a three-dimensional cloud-ensemble model. *Quarterly Journal of the Royal Meteorological Society*, *124*(550), 2073–2097. https://doi.org/10.1002/qj.49712455013

Tompkins, A., & Semie, A. (2017). Organization of tropical convection in low vertical wind shears: Role of updraft entrainment. *Journal of Advances in Modeling Earth Systems*, *9*(2), 1046–1068. https://doi.org/10.1002/2016MS000802

Tompkins, A., & Semie, A. (2021). Impact of a mixed ocean layer and the diurnal cycle on convective aggregation. *Journal of Advances in Modeling Earth Systems*, *13*(12), e2020MS002186. https://doi.org/10.1029/2020MS002186

Virtanen, P., Gommers, R., Oliphant, T. E., Haberland, M., Reddy, T., Cournapeau, D., et al. (2020). SciPy 1.0: Fundamental algorithms for scientific computing in Python. *Nature Methods*, *17*(3), 261–272. https://doi.org/10.1038/s41592-019-0686-2

Weverberg, K. V., Vogelmann, A. M., Lin, W., Luke, E. P., Cialella, A., Minnis, P., et al. (2013). The role of cloud microphysics parameterization in the simulation of mesoscale convective system clouds and precipitation in the tropical Western Pacific. *Journal of the Atmospheric Sciences*, *70*(4), 1104–1128. https://doi.org/10.1175/JAS-D-12-0104.1

Windmiller, J., & Craig, G. (2019). Universality in the spatial evolution of self-aggregation of tropical convection. *Journal of the Atmospheric Sciences*, *76*(6), 1677–1696. https://doi.org/10.1175/JAS-D-18-0129.1

Wing, A. A. (2019). Self-aggregation of deep convection and its implications for climate. *Current Climate Change Reports*, *5*(1), 793–813. https://doi.org/10.1007/s40641-019-00120-3

Wing, A. A., & Cronin, T. (2016). Self-aggregation of convection in long channel geometry. *Quarterly Journal of the Royal Meteorological Society*, *142*(694), 1–15. https://doi.org/10.1002/qj.2628

Wing, A. A., Emanuel, K., Holloway, C. E., & Muller, C. (2018). Convective self-aggregation in numerical simulations: A review. In R. Pincus, D. Winker, S. Bony, & B. Stevens (Eds.), *Shallow clouds, water vapor, circulation, and climate sensitivity* (pp. 1–25). Springer International Publishing. https://doi.org/10.1007/978-3-319-77273-8_1

Wing, A. A., & Emanuel, K. A. (2014). Physical mechanisms controlling self-aggregation of convection in idealized numerical modeling simulations. *Journal of Advances in Modeling Earth Systems*, *6*(1), 59–74. https://doi.org/10.1002/2013MS000269

Wing, A. A., Reed, K. A., Satoh, M., Stevens, B., Bony, S., & Ohno, T. (2018). Radiative–convective equilibrium model intercomparison project. *Geoscientific Model Development*, *11*(2), 793–813. https://doi.org/10.5194/gmd-11-793-2018

Wing, A. A., Stauffer, C. L., Becker, T., Reed, K. A., Ahn, M.-S., Arnold, N. P., et al. (2020). Clouds and convective self-aggregation in a multimodel ensemble of radiative-convective equilibrium simulations. *Journal of Advances in Modeling Earth Systems*, *12*(9), e2020MS002138. https://doi.org/10.1029/2020MS002138

Yanase, T., Nishizawa, S., Miura, H., Takemi, T., & Tomita, H. (2020). New critical length for the onset of self-aggregation of moist convection. *Geophysical Research Letters*, *47*(16), e2020GL088763. https://doi.org/10.1029/2020GL088763

Yang, D. (2018). Boundary layer diabatic processes, the virtual effect, and convective self-aggregation. *Journal of Advances in Modeling Earth Systems*, *10*(9), 2163–2176. https://doi.org/10.1029/2017ms001261

Yang, D. (2019). Convective heating leads to self-aggregation by generating available potential energy. *Geophysical Research Letters*, *46*(17–18), 10687–10696. https://doi.org/10.1029/2019GL083805

Yao, L., Yang, D., & Tan, Z.-M. (2022). A vertically resolved MSE framework highlights the role of the boundary layer in convective self-aggregation. *Journal of the Atmospheric Sciences*, *79*(6), 1615–1631. https://doi.org/10.1175/JAS-D-20-0254.1